Chemical Engineering Science 332 (2026) 124172

Contents lists available at ScienceDirect

Chemical Engineering Science

journal homepage: www.elsevier.com/locate/ces

Modeling of catalytic partial oxidation and dry reforming of CH_4 in fixed-bed reactors: Comparison of 3D particle-resolved (PRCFD) and 1D simulations

Akash Shirsath [a], Matthias Hettel [a,*], Eric A. Daymo [b], Martin Kutscherauer [c], Olaf Deutschmann [a]

[a] Institute for Chemical Technology and Polymer Chemistry (ITCP), Karlsruhe Institute of Technology (KIT), Engesserstraße 22, 76131 Karlsruhe, Germany
[b] Tonkomo, LLC, Gilbert, AZ 85297, United States
[c] Institute for Chemical Process Engineering (CVT), Karlsruhe Institute of Technology (KIT), Fritz-Haber-Weg 2, 76131 Karlsruhe, Germany

ARTICLE INFO

Keywords:
Modeling of fixed-beds
Catalytic fixed-bed reactors
1D pseudo-continuum model
Particle-resolved computational fluid dynamics (PRCFD)
Surface chemistry microkinetics
Slender beds

ABSTRACT

This work compares a detailed 3D particle-resolved CFD model and a 1D pseudo-continuum model for catalytic fixed-bed reactors for three different tube-to-particle diameter ratios (1.1/2/7) over a wide range of particle Reynolds numbers (29/145/290/1450). Dry reforming of methane and catalytic partial oxidation are simulated using microkinetics mechanisms in both frameworks. In the 1D model, over 100 combinations of literature correlations for heat and mass transfer and overall heat transfer coefficients are evaluated against 3D reference solutions. The study shows that no universal correlation set is valid. Instead, the best choice of correlations for the 1D model depends on bed geometry and reaction type. The results delineate conditions where simplified 1D models remain reliable and where fully resolved CFD becomes necessary for reactor design and analysis.

1. Introduction

Fixed bed reactors are used for a wide range of heterogeneously catalyzed processes and are an important part of the chemical industry (Eigenberger et al., 1997). Many of these processes entail highly exothermic reactions as Catalytic Partial Oxidation (CPOX) of methane (e.g., (Deutschmann and Schmidt, 1998; Schwiedernoch et al., 2003) or endothermic reactions as Dry Reforming of Methane (DRM) (e.g., (Giehr et al., 2020), necessitating rigorous temperature control to ensure safe operation and optimal performance (Dixon and Wu, 2020). For such processes, slender fixed-bed reactors with only a few particles along the tube diameter are used to remove and supply the reaction heat sufficiently, while keeping the pressure drop at a moderate level. The small tube-to-particle diameter ratio ($d_t/d_p < 7$) results in a pronounced effect of the tube wall on the arrangement of particles in the tube, leading to an inhomogeneous morphology (Ziółkowska and Ziółkowski, 1988). This morphology impacts fluid flow (Giese et al., 1998), heat and species mass transport (Dixon, 2021a;b), and reaction kinetics (Kutscherauer et al., 2024). Capturing these local structural effects in reactor models is challenging, but crucial for reliable predictions of slender fixed–bed performance (Freund et al., 2005).

The usual reaction engineering model describes the tubular catalytic fixed bed as a pseudo-continuum discretized in axial (1D) or axial and radial (2D) direction, upon which the governing equations for energy and species mass balances are solved (Froment et al., 2011). Pseudo-continuum models are divided into pseudo-homogeneous and heterogeneous models. In pseudo-continuum models, the particles and fluid are combined in one phase. Heterogeneous reactor models consist of separate conservation equations for fluid and catalyst particles, which are coupled with appropriate closure equations (Froment et al., 2011). Heat and mass transport is implemented employing effective transport parameters calculated from semi-empirical correlations (Stegehake et al., 2019). The combination of simplifying assumptions regarding the geometric structure and the lack of effective transport parameter correlations in the pseudo-continuum models may result in inaccurate predictions, particularly for an inhomogeneous packed bed morphology in slender fixed-bed reactors (Dixon, 2021a). Most of the correlations for effective mass and heat transport were developed based on experiments performed in packed beds without chemical reaction. Since the correlations are only valid for the conditions of the experiments to which they

* Corresponding author.
E-mail address: matthias.hettel@kit.edu (M. Hettel).

https://doi.org/10.1016/j.ces.2026.124172
Received 12 March 2026; Received in revised form 30 April 2026; Accepted 4 May 2026
Available online 5 May 2026

were adapted, their applicability to reactive systems is questionable and needs to be further studied. Moreover, Flaischlen et al. (Flaischlen and Wehinger, 2019) have demonstrated that the morphology of slender packed beds ($d_t/d_p < 7$), whether consisting of spheres or rings, undergo a significant transformation for minor changes in the d_t/d_p-ratio. This results in scattered values for the void fraction and the pressure drop depending on the d_t/d_p-ratio, which cannot be predicted by the monotone functions that are currently available in the literature (Flaischlen and Wehinger, 2019). Similar findings have been reported by Dixon for slender fixed bed of spheres regarding heat transport (Dixon, 2021b). The author has recommended the principal use of Particle-Resolved Computational Fluid Dynamics (PRCFD) simulations for slender fixed-bed reactors.

PRCFD simulation has emerged as the most detailed approach for modeling catalytic fixed-bed reactors in recent years (Jurtz et al., 2019). In contrast to the classical pseudo-continuum models, PRCFD simulations do not rely on effective transport correlations, as the spatial domain is fully resolved and every single particle is accounted for when solving the governing equations for momentum, mass, energy, and species balances (Dixon and Partopour, 2020). The underlying packed bed geometries are typically generated synthetically using either the Discrete Element Method (DEM) or the Rigid Body Approach (RBA) (Flaischlen and Wehinger, 2019; Jurtz et al., 2019; Partopour and Dixon, 2017). The governing equations are solved by discretizing the 3D geometry using the Finite Volume or Lattice-Boltzmann methods, although the latter is less commonly applied. In PRCFD simulations, catalytic reactions can be incorporated as heat and species mass fluxes at the particle surface and pore diffusion can be considered using an effectiveness factor (Wehinger et al., 2017). When intra-particle concentration gradients become dominant, transport and reaction within the porous catalyst can be modeled using a pseudo-continuum approach, which is coupled to the surrounding fluid flow via conjugated heat and mass transfer models (Kutscherauer et al., 2024; Dixon et al., 2010; Maffei et al., 2016). Finally, incorporating microkinetics into the PRCFD approach can lead to a more thorough understanding of the relationship between fluid flow and reactions (Wehinger et al., 2022). However, a full coupling between PRCFD and microkinetics is not computationally feasible due to the wide range of different length and time scales, especially in nanoporous catalysts (Bukowski et al., 2021). Therefore, microkinetics and PRCFD must be solved separately, and relevant information must be transferred between the different scales. Different strategies for a computationally efficient and physically accurate incorporation of microkinetics into PRCFD simulations are available in literature. Chemical acceleration techniques, such as in-situ Adaptive Tabulation (ISAT) (Pope, 1997) or Cell Agglomeration (Babajimopoulos et al., 2005) try to reduce computational costs in the calculation of the reaction rates. An alternative methodology is to derive computationally efficient surrogate models based on data generated by microkinetics models, which can be directly implemented in the PRCFD simulation (Döppel and Votsmeier, 2022). Bracconi and Maestri (Bracconi and Maestri, 2020) used machine learning to generate a surrogate model of detailed chemistry and employed it in the CFD (Computational Fluid Dynamics) simulation of a catalytic open-cell foam. Biermann et al. used a global reaction neural network to efficiently compute microkinetics in a simulation of an industrial packed bed reactor (2,400 particles) for methane steam reforming with PRCFD (Biermann et al., 2025). However, PRCFD coupled with microkinetics remains computationally demanding, especially for industrial-scale reactors of several meters in length, consisting of thousands of complexly shaped particles. Therefore, the application of computationally efficient pseudo-continuum models is still relevant for reactor design and reaction monitoring. Nevertheless, PRCFD is an important method for developing improved correlations for effective transport parameters and investigating the limitations of pseudo-continuum models (Dixon, 2026). Recently, several authors demonstrated that pseudo-continuum models can reflect the results of detailed PRCFD simulations when PRCFD is employed to derive effective transport parameters (Anderson et al., 2023; Hernandez-Aguirre et al., 2025; Liu et al., 2023; Weng et al., 2025; Xavier et al., 2026). Nevertheless, the question of whether the effective transport parameters are independent of ongoing chemical reactions remains elusive.

In this contribution, over 100 combinations of literature correlations for effective fluid–solid heat and mass transfer parameters as well as for the overall heat transfer coefficient between packed bed and tube wall are tested in a 1D pseudo-continuum model. Since the focus of the presented work is to investigate external transport phenomena, internal heat and mass transport effects are not considered in the 1D and 3D models. The models are used to calculate catalytic fixed-bed reactors with d_t/d_p-ratios ranging from 1.1 to 7.0 and particle Reynolds numbers $\left(Re = \frac{u_{in} \bullet d_p}{\nu_{in}}\right)$ ranging from 29 to 1450. As reactions the endothermic Dry Reforming of Methane (DRM) and the exothermic Catalytic Partial Oxidation (CPOX) of methane are studied. For both processes, microkinetics is used to calculate the reaction rates. The 1D pseudo-continuum results for all tested combinations of transport parameter correlations are compared for all cases with detailed PRCFD simulations coupled with the same microkinetics expressions as the 1D model using the mean-field approximation approach (Benzinger et al., 2019). By investigating different reaction systems, this work addresses the question of whether the choice of effective transport parameter correlations is affected by chemical reactions, rather than only by the d_t/d_p-ratio and process conditions.

2. Methods

In this section, the computational methods used for the present study are introduced. In Section 2.1 the use of detailed surface chemistry in both CFD and the 1D model is addressed. In Section 2.2, the heat-transfer correlations used in the 1D modeling are presented, followed by a description of the program PBR (Packed Bed Reactor). This is part of the DETCHEM^{TM} suite (Deutschmann et al., 2014). In Section 2.3 the CFD code DUO and the numerical setup for 3D modeling are explained.

2.1. CFD and heterogeneous microkinetics

2.1.1. Mean-field approach

The description of surface reactions is analogous to descriptions of gas-phase reactions. However, since there exist almost innumerable numbers of different surface structures, only little is known about the exact reaction paths. Instead of looking at interactions between single adsorbed species the mean-field approximation is a common choice for modeling (Hettel et al., 2018; Kee et al., 2003). Additional details on the implementation of the mean-field approximation can be found in (Daymo et al., 2022; Hettel et al., 2018; Hettel et al., 2015).

For PRCFD, the most time-consuming step is often the calculation of the total molar production rate $\dot{s}_i$ of a gaseous species or an adsorbed surface species. $\dot{s}_i$ is calculated as a product of rate coefficients and concentrations determined by:

$$\dot{s}_i = \sum_{k=1}^{K_s} \nu_{ik} k_{fk} \prod_{i=1}^{N_g+N_s+N_b} c_i^{\nu'_{ik}} \left(i = 1, \cdots, N_g + N_s + N_b\right). \quad (1)$$

Here, K_s is the number of surface reactions (including adsorption and desorption) among N_g gas-phase, N_s surface and N_b bulk species (species for which no conservation equation is solved), ν_{ik} are the stoichiometric coefficients, c_i are the concentrations of adsorbed gaseous and bulk species, and k_{fk} are the forward rate coefficients described by an Arrhenius expression.

Typically, the total molar production rate ($\dot{s}_i$, in mol/m^2/s) is obtained by solving the series of parallel Ordinary Differential Equations

(ODE's) that describe the reaction rates (Eq. (1). Solving the chemical source term in this way is also called direct integration. This determination of the surface chemical source terms, when repeated for every reactive face in a fixed bed with many resolved 3D particles, can be the slowest step in a reactive flow CFD simulation. It is therefore desirable to utilize approaches that reduce the calculation time to obtain the chemical source term of each species.

The net surface reaction rate $\dot{s}_i$ is assembled by finding the net production rate of species i as a linear combination of the applicable rates in the reaction mechanism. After calculating $\dot{s}_i$, the flux of species j_i (in kg/(m^2·s)) at the interface between fluid and the outer geometrical surface of the washcoat/catalyst is given by:

$$\boldsymbol{j_i = \dot{s}_i \bullet M_i \bullet F_{cat/geo} \bullet \eta_i} \tag{2}$$

M_i is the molecular weight of species i and $F_{cat/geo}$ is the ratio of catalytically active surface area to geometric surface area. For purposes of this paper in which non-porous particles without any catalyst located inside the particles are considered, this is the external surface area, but when internal pore diffusion is considered, $F_{cat/geo}$ can include the internal surface area as well. The effectiveness factor η_i is the ratio of the reaction rate to the rate that would occur without internal diffusion limitations inside porous washcoats or particles. This factor is based on the Thiele modulus which includes the following parameters: concentration of the species at the boundary between fluid and washcoat, washcoat thickness and effective diffusion coefficient in a porous substrate (Deutschmann, 2011). For purposes of the present study, $\eta_i = 1$. The product $(F_{cat/geo} \bullet \eta_i)$ is used in the CFD approach to simultaneously account for active catalytic surface area and internal diffusion limitation and is represented by the term $F_{cat/geo}$ in subsequent sections.

2.1.2. Microkinetics models

In the methane Catalytic Partial Oxidation (CPOX) process, synthesis gas (a mixture of H_2 and CO) is produced from CH_4 and O_2 in a heterogeneously catalyzed reaction. Although a detailed mechanism was used in this work, the global reaction is given here to point out the influence of the operational conditions

$$\boldsymbol{CH_4 + \frac{1}{2}O_2 = CO + 2H_2} \tag{3}$$

The operational conditions are set by the C/O ratio. This is defined as the ratio of the total number of carbon atoms and the total number of oxygen atoms in the reactant feed. The stoichiometric composition for partial oxidation corresponds to C/O = 1.0. For these conditions a CPOX reformer operates in an autothermal mode (no external heating is required). The multi-step surface reaction mechanism used for this work was developed for the partial oxidation and autothermal reforming of methane over rhodium (Deutschmann et al., 2001). The mechanism includes 7 gas phase species (CH_4, O_2, H_2, H_2O, CO, CO_2, N_2), 11 surface species (H_2O, H, O, OH, CO, C, CH_3, CH_2, CH, CO_2, CH_4) and 38 reactions. For the active-site density of Rhodium, the value of $\Gamma = 2.72 \bullet 10^{-9}$ mol/cm^2 is used. The $F_{cat/geo}$ ratio for CPOX cases is set to 5.64, the same value used by Hettel et al. (Hettel et al., 2018; Hettel et al., 2015). This value is somewhat arbitrary for this analysis of chemical acceleration methods because there is no direct comparison to experimental data. The full CPOX mechanism is given in the Supplemental Information (Table S1).

Meanwhile, for Dry Reforming of Methane (DRM), synthesis gas is produced from the reaction of methane and CO_2 in a heterogeneously catalyzed reaction. Although a detailed mechanism was used in this work, the global reaction scheme for DRM is given here

$$\boldsymbol{CH_4 + CO_2 = 2CO + 2H_2} \tag{4}$$

A multi-step surface reaction mechanism was used, which was developed for the methane reforming and oxidation over nickel (Delgado et al., 2015). The mechanism includes 6 gas phase species (CH_4, O_2, H_2, H_2O, CO, CO_2), 13 surface species (H_2O, H, O, OH, CO, C, CH_3, CH_2, HCO, COOH, CH, CO_2, CH_4) and 52 reactions. For active-site density, a value of $\Gamma = 2.66 \bullet 10^{-9}$ mol/cm^2 was chosen. The $F_{cat/geo}$ ratio for DRM cases is set to 90, the same value used by Wehinger et al. (Wehinger et al., 2016) for previous 3D resolved bed CFD studies.

The full DRM mechanism is given in the Supplemental Information (Table S2). It is noted that this mechanism was successfully implemented by Wehinger et al. (Wehinger et al., 2016) to match experimental data in a 3D resolved particle CFD simulation.

2.2. 1D modeling of packed bed reactors

The 1D packed-bed reactor simulations were conducted using a pseudo-continuum modeling approach for the fixed bed implemented within the DETCHEM^{TM} software package (Deutschmann et al., 2014). As is required for a 1D model, the radial gradients of fluid properties were neglected. This leads to the following set of simplified one-dimensional governing equations for mass, species, heat, and momentum balances. Firstly, Eq. (5) shows the steady continuity equation. On the left-hand side, z is the axial coordinate, ρ the density, u the velocity. On the right-hand side i is the gas phase species, M_i their molecular weight, $\dot{s}_i$ the net surface reaction rate and a_v the specific surface area per volume of bed in *[1/m]*. When there is no deposition or gasification of mass to/from the surface (respectively) the right-hand side term of Eq. (5) is equal to zero.

$$\boldsymbol{\frac{d(\rho u)}{dz} = a_v \bullet \sum_{i \in S_g} M_i \dot{s}_i \left[\frac{kg}{m^3 \bullet s}\right]} \tag{5}$$

The species mass balance is given in Eq. (6). Y_i is the mass fraction of species i. Axial diffusion is not modeled. This assumption is generally valid when $Pe_{mass} = L \bullet u/D$ for the most diffusive species is > 100, and is oftentimes valid when $Pe_{mass} > 10$. Here D is the species mass diffusion coefficient (m^2/s), and L is the reactor length. For the current study, the lowest values of Pe_{mass} for inlet conditions at the lowest Re_p value tested are 71.1 for CH_4 (CPOX) and 86.5 for CH_4 (DRM).

$$\boldsymbol{\rho u \frac{dY_i}{dz} = a_v M_i \dot{s}_i - a_v Y_i \bullet \sum_{j \in S_g} M_j \dot{s}_j \left[\frac{kg}{m^3 \bullet s}\right]} \tag{6}$$

To account for interphase mass transport phenomena, Eq. (7) introduces an external fluid–solid mass transfer coefficient external fluid–solid mass transfer coefficient ($k_{fs,i}$), which quantifies the resistance between the bulk gas-phase composition and the catalyst surface. As will be discussed in Section 3, the effect of external mass transfer (Eq. (7)) was enabled for all CPOX cases, but disabled for all DRM cases. PBR includes various empirical correlations for the calculation of $k_{fs,i}$ (discussed in Section 2.2.1).

$$\boldsymbol{M_i \dot{s}_i = k_{fs,i}(\rho_{s,i} Y_{s,i} - \rho_i Y_i) \left[\frac{kg}{m^3 \bullet s}\right]} \tag{7}$$

The energy balance for the gas phase is shown in Eq. (8), where T is the gas phase temperature, T_s the temperature of the solid surface, T_w the temperature of the tube wall, $C_{p,i}$ the species heat capacity. U is the overall heat transfer coefficient into radial direction (see Section 2.2.1), d_t is the diameter of the tube and h_{fs} the heat transfer coefficient between gas phase and solid particle surface.

$$\boldsymbol{\rho u \sum_{i \in S_g} Y_i C_{p,i} \frac{dT}{dz} = \frac{4}{d_t} U(T_w - T) - h_{fs} a_v (T_s - T) \left[\frac{W}{m^3}\right]} \tag{8}$$

Axial conduction is not modeled, which is generally valid when $Pe_{heat} = L \bullet u/\alpha$ is > 100, and is oftentimes valid when $Pe_{heat} > 10$. Here α is the thermal diffusivity of the mixture. At the lowest Re_p evaluated in the

present work, at inlet conditions $Pe_{heat} = 74.8$ for CPOX and 86.4 for DRM.

The energy balance for the solid phase is shown in Eq. (9). When the solid energy balance is enabled, the reactor model is heterogeneous, as described in Section 1. However, whenever the solid energy balance is disabled the fluid and solid temperatures are in equilibrium, implying $T_s = T$. As will be discussed in Section 3, initial testing under adiabatic conditions found that the solid energy balance was of secondary importance for the tested DRM and CPOX cases. It further is noted that Nu_{fs}, from which h_{fs} is calculated, is used in the calculation of one of the methods for the wall Nusselt number, Nu_w (Section 2.2.3.1, Method 1, Dixon-Cresswell), even when $T_s = T$.

$$h_{fs}a_v(T_s - T) = a_v\sum_{i\in S_g} h_i\dot{s}_i\left[\frac{W}{m^3}\right] \tag{9}$$

The pressure drop in the reactor is calculated via the Ergun equation (Ergun, 1952) (Eq. (10)). Here p is the pressure, d_p the particle diameter, μ the dynamic viscosity and ϵ the void fraction of the bed. The Ergun equation is not strictly applicable at $Re_p = 1450$, but for the relatively short beds of spherical particles (110 cm in length) evaluated in the present study, the pressure drop is low and the comparison between 1D and 3D remains unaffected.

$$\frac{dp}{dz} = -\frac{\rho u^2}{d_p}\left(\frac{(1-\epsilon)}{\epsilon^3}\right)\left[150\frac{(1-\epsilon)\mu}{\rho u d_p} + 1.75\right]\left[\frac{Pa}{m}\right] \tag{10}$$

2.2.1. Heat transport in a fixed bed inside a tube

Heat distribution in fixed-bed reactor tubes arises from several concurrent mechanisms, including thermal conduction in both the solid and fluid phases, as well as convective heat transfer between the fluid, the particle surfaces, and the inner tube wall. To represent these mechanisms within a one-dimensional framework, empirical correlations are required. Fig. 1 summarizes the hierarchy of the correlations employed in this work.

According to Eq. (8) the overall heat-transfer coefficient U combines all contributions to the radial transport of heat from tube wall through the packed bed. The fluid–solid heat transfer coefficient, h_{fs}, controls heat interchange between gas phase and solid particles.

The following sections present a stepwise discussion of the individual heat transport mechanisms and the corresponding correlations. In this context, Fig. 1 serves as a roadmap indicating the dependencies and interactions among the various correlations used in the model.

2.2.2. Conductive heat transfer

2.2.2.1. Effective radial bed (solid plus stagnant fluid) thermal conductivity k_{rb}. The effective radial thermal conductivity of the bed k_{rb} includes both the conduction in solid particles and the conduction in stagnant fluid (zero velocity). Note that in some publications, e.g. (Zehner and Schlünder, 1970);k_{rb} is referred to as k_{rs}. One k_{rb} model additionally includes the effect of radiative heat transfer between particle surfaces. We evaluated five models for the effective radial solid thermal conductivity k_{rb}, summarized in Table 1. The detailed description of these five methods follows.

k_{rb} Method 1: Zehner–Schlünder effective radial bed conductivity.

The Zehner–Schlünder (Zehner and Schlünder, 1970) model treats heat flow in the packed bed as a combination of parallel and series paths through the solid grains and interstitial fluid. For spherical particles it gives, as shown in Eq. (11):

$$k_{rb} = k_f\left(\left(1-\sqrt{1-\epsilon}\right) + \sqrt{1-\epsilon}\left\{\frac{2}{1-\frac{k_f}{k_s}B}\left[\frac{\left(1-\frac{k_f}{k_s}\right)B}{\left(1-\frac{k_f}{k_s}B\right)^2}\ln\frac{k_s}{k_f B} - \frac{B+1}{2} - \frac{B-1}{1-\frac{k_f}{k_s}B}\right]\right\}\right) \tag{11}$$

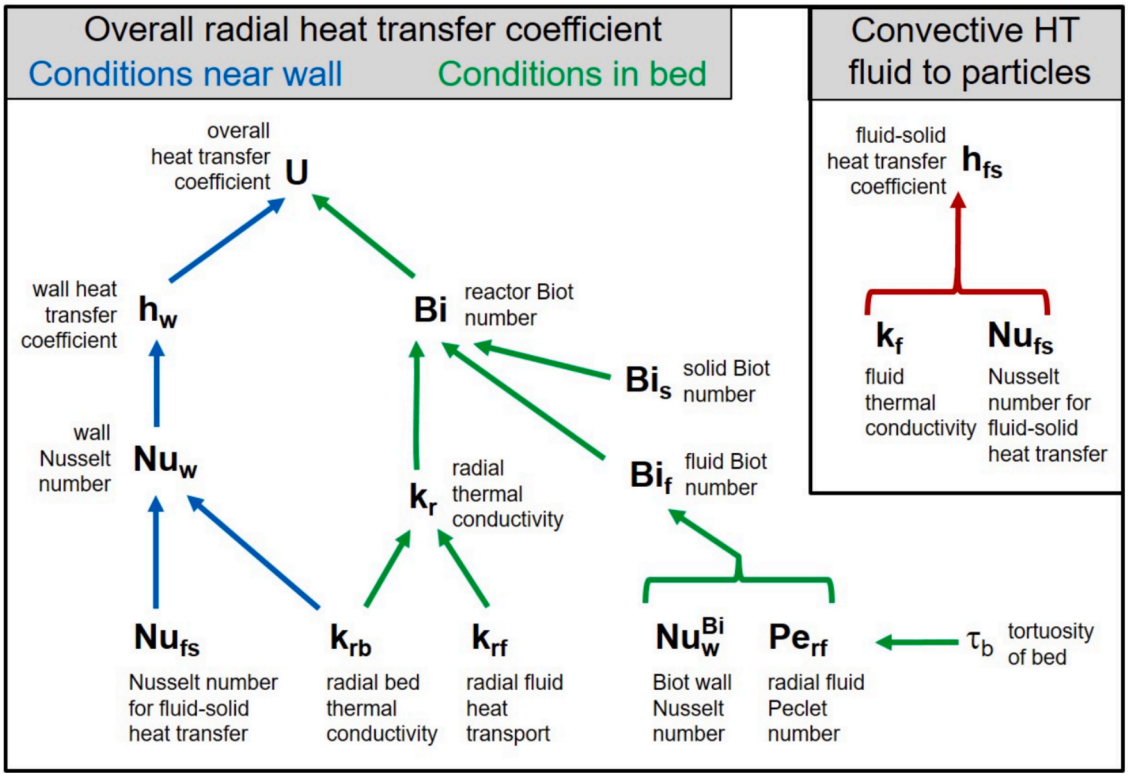

Fig. 1. Principal hierarchy of heat-transfer (HT) correlations employed in this work. Note that not all correlations follow exactly the same pathway.

Table 1
Correlations for radial solid thermal conductivity, k_{rb}, evaluated in this work.

Method Name	Key Idea / Origin
Zehner–Schlünder model (Method 1)	Series/parallel conduction paths through solid and fluid for spheres; matches pure-fluid and solid limits; validated for moderate porosity
Specchia–Baldi stagnant-conductivity fit (Method 2)	Simplified algebraic fit for stagnant conduction, correlated to extensive data across porosity and conductivity ratios
Bauer–Schlünder (with radiative correction) (Method 3)	Refined Zehner–Bauer–Schlünder conduction term plus a lumped radiative conductivity k_{rad} for high-temperature beds
Kunii–Smith stagnant-conductivity model (Method 4)	Uses an effective pellet length l_v related to conductivity ratio and porosity to compute stagnant bed conductivity
Radiation-corrected Kunii–Smith (Method 5)	Kunii–Smith conduction plus additional radiative conductances in solid and void phases to capture high-temperature effects

where $B = 1.25((1-\epsilon)/\epsilon)^{10/9}$. This expression correctly collapses to the pure-fluid limit ($\epsilon \to 1$) and to the solid-matrix limit ($\epsilon \to 0$) and has been validated against experimental data for moderate $\epsilon \approx 0.3 - 0.5$ to within ± 15%.

***k_{rb}* Method 2**: Specchia–Baldi effective radial bed conductivity.

Rather than the full Zehner–Schlünder formula Eq. (11), Specchia et al. (Specchia et al., 1980) proposed a simpler algebraic form for the stagnant (pure-conduction) contribution of the packed-bed conductivity

$$k_{rb} = k_f\left[\epsilon + \frac{\beta(1-\epsilon)}{\phi + (k_f\gamma/k_s)}\right] \tag{12}$$

with $\beta = 1$, $\gamma = 2/3$, and $\phi = 0.22\,\epsilon^2$. Specchia et al. (Specchia et al., 1980) fitted Eq. (26) to over 200 datasets spanning $\epsilon \approx 0.3 - 0.5$, $N \approx 5 - 25$ and conductivity ratios of 10 − 8000, reporting mean deviations under ± 12%.

***k_{rb}* Method 3**: Bauer–Schlünder effective radial bed conductivity with radiative correction

The core conduction term in Eq. (13) is the well-established Zehner–Bauer–Schlünder model for stagnant packed-bed conductivity, which Bauer & Schlünder (Bauer and Schlunder, 1978) refined. It treats heat flow through contacting particles as a combination of series and parallel paths, yielding

$$k_{rb} = k_f\left((1-\sqrt{1-\epsilon}) + \sqrt{1-\epsilon}\left\{\frac{2}{1-\frac{k_f}{k_s}B}\left[\frac{\left(1-\frac{k_f}{k_s}\right)B}{\left(1-\frac{k_f}{k_s}B\right)^2}\ln\frac{k_s}{k_fB} - \frac{B+1}{2} - \frac{B-1}{1-\frac{k_f}{k_s}B}\right]\right\}\right) + k_{rad}, \tag{13}$$

with $B = 1.25(\frac{1-\epsilon}{\epsilon})^{10/9}$. To account for interstitial thermal radiation at elevated temperatures, a lumped radiative conductivity k_{rad} is added (Eq. (14)),

$$k_{\text{rad}} = k_f\left((1-\sqrt{1-\epsilon})\right)\frac{k_R}{k_f} + \sqrt{1-\epsilon}\left(\frac{k_f}{k_R}\frac{k_f}{k_s}\right)^{-1}\Bigg) \tag{14}$$

where k_R, is the term associated with radiation (Eq. (15)), where e is the emissivity (e set to 1 for the present work). It is noted that even though that this method (along with k_{rb} Method 5) includes radiation effects, the CFD calculations do not.

$$\frac{k_R}{k_f} = 2.27x10^{-7}\left(\frac{e}{2-e}\right)T_f^3\frac{d_p}{k_f} \tag{15}$$

***k_{rb}* Method 4**: Kunii–Smith effective radial bed conductivity

Kunii and Smith (Kunii and Smith, 1960) derived an explicit expression for the pure-conduction (stagnant fluid) thermal conductivity of a rigid packed bed by relating the effective pellet thickness (l_v) to the solid-to-fluid conductivity ratio (Eq. (16)). They first define two auxiliary functions (Eq. (17)-(18)):

$$\kappa = \frac{k_s}{k_f} \tag{16}$$

$$\phi_1 = \frac{0.333\left(1-\frac{1}{\kappa}\right)^2}{\ln\{\kappa - 0.577(\kappa-1)\} - 0.423\left(1-\frac{1}{\kappa}\right)} - \frac{2}{3\kappa} \tag{17}$$

and,

$$\phi_2 = \frac{0.072\left(1-\frac{1}{\kappa}\right)^2}{\ln\{\kappa - 0.925(\kappa-1)\} - 0.075\left(1-\frac{1}{\kappa}\right)} - \frac{2}{3\kappa} \tag{18}$$

Then the dimensionless pellet length (l_v/d_p) is interpolated by porosity, as shown in Eq. (19):

$$\frac{l_v}{d_p} = \begin{cases} \phi_2, \epsilon < 0.26 \\ \phi_2 + (\phi_1 - \phi_2)\dfrac{\epsilon - 0.26}{0.476 - 0.26}, \; 0.26 \le \epsilon \le 0.476 \\ \phi_1, \epsilon > 0.476 \end{cases} \tag{19}$$

and the stagnant conductivity (Eq. (20))

$$\frac{k_{rb}}{k_f} = \epsilon + \left[\frac{(1-\epsilon)}{\frac{1}{d_p/l_v} + \frac{2}{3\kappa}}\right] \tag{20}$$

This model requires only the porosity, the conductivity ratio κ, and the particle size and matches classic experimental data for $\epsilon \approx 0.3 - 0.5$, $\kappa \approx$ 1–100, and $d_p/d_t \approx$ 5–20 to within about ± 10%.

***k_{rb}* Method 5**: Radiation-corrected Kunii–Smith model.

To capture radiative transfer at high temperature, Kunii & Smith (Kunii and Smith, 1960) added a radiative conductance term, in addition to Eq. (16)-(19)(17(17):

$$\frac{k_{rb}}{k_f} = \epsilon\left[1 + \frac{h_{rv}}{d_p}\right] + \left[\frac{(1-\epsilon)}{\frac{1}{d_p/l_v + d_p h_{rs}/k_f} + \frac{2}{3\kappa}}\right] \tag{21}$$

where,

$$h_{rs} = 2.27x10^{-7}\left(\frac{e}{2-e}\right)T_f^3\frac{d_p}{k_f}, \tag{22}$$

$$h_{rv} = 2.27x10^{-7}\left[1 + \frac{e}{2(1-\epsilon)}\frac{1-e}{e}\right]T_f^3. \tag{23}$$

Here h_{rs} and h_{rv} are equivalent radiative heat-transfer coefficients in the solid and void. T_f is the fluid temperature, and e set to 1 for the present work. This radiation-augmented form has been shown to improve agreement with high-temperature packed-bed data by up to + 20% for$T_f > 500$ K (Kunii and Smith, 1960).

2.2.2.2. Radial fluid thermal conductivity k_{rf} . The radial fluid thermal conductivity includes the effect of turbulent mixing in the radial direction. The effect of pure conduction in stagnant fluid is incorporated in the effective radial solid thermal conductivity k_{rb} above. We evaluated

four radial fluid thermal conductivity models, k_{rf}, summarized in Table 2. The detailed description of these four methods follows.

k_{rf} Method 1: Yagi–Wakao turbulent-mixing model.

In packed beds the fluid's contribution to radial heat conduction is dominated by turbulent mixing rather than molecular diffusion. Yagi and Wakao (Yagi and Wakao, 1959) showed, Eq. (34), that this can be captured by treating the eddy thermal conductivity as proportional to the free-stream conductivity times a dimensionless mixing parameter.

$$k_{\mathrm{rf}} = k_f\left(\frac{\mathbf{Pr}\bullet \mathbf{Re_p}}{\mathbf{Pe}_{rf}}\right) \tag{24}$$

Here Pe_{rf} is the radial Peclet number for the fluid. This form ensures that at low velocities ($\mathrm{Re_p}\to 0$) the radial conductivity vanishes ($k_{\mathrm{rf}}\to 0$), while at large velocities ($\mathrm{Re_p}\to\infty$) the turbulent conductivity grows in proportion to the turbulent mixing rate.

k_{rf} Method 2: Specchia–Baldi wall-mixing model.

Specchia et al. (Specchia et al., 1980) proposed an explicit form for the fluid's eddy conductivity near the wall by combining the classic Prandtl–Reynolds scaling with a geometric correction for proximity to the tube wall, as shown in Eq. (25)

$$k_{\mathrm{rf}} = k_f\left[\frac{\mathbf{Pr}\bullet \mathbf{Re}_a}{8.65\left(1+19.4(d_{p,a}/d_t)^2\right)}\right], \tag{25}$$

where Re_a is based on the particle diameter $\mathrm{d}_{p,a}$, defined as the diameter of a sphere with the same surface area as the particle. By fitting over both literature and new data (for $\epsilon \approx 0.35 - 0.45$, $d_{pa}/d_t \approx 1 - 100$, and $\mathrm{Re}_a \approx 10 - 1000$), Specchia et al. (Specchia et al., 1980) showed that this one-term expression reproduces the fluid's radial mixing conductivity to within ± 10% across typical packed-bed conditions.

k_{rf} Method 3: Bauer–Schlünder wall-mixing correction

Bauer and Schlünder (Bauer and Schlunder, 1978) provided a simple expression for the fluid's turbulent conductivity as a function of the local Reynolds number based on an effective mixing length x_f, as shown in Eq. (26):

$$k_{\mathrm{rf}} = k_f\left(\frac{\mathbf{Pr}\bullet \mathbf{Re}_x}{8\left\{2-[1-(2/N)]^2\right\}}\right) \tag{26}$$

where $\mathrm{Re}_x = \rho x_f u/\eta$ and $x_f = 1.15\ d_p$. Bauer & Schlünder showed that this one-term form reproduces the radial mixing conductivity to within ± 12% for $N \approx 3 - 12$, and $\mathrm{Re_p} \approx 100 - 1000$.

k_{rf} Method 4: Winterberg–Tsotsas high-Pe limit.

Winterberg et al. (Winterberg et al., 2000) proposed a simple, single-term expression for the fluid's eddy conductivity in the limit of high radial Peclet numbers, shown in Eq. (27).

Table 2
Correlations for radial fluid thermal conductivity, k_{rf}, evaluated in this work.

Method Name	Key Idea / Origin
Yagi–Wakao turbulent-mixing model (Method 1)	Eddy thermal conductivity proportional to $k_f \cdot \mathrm{Re_p}/\mathrm{Pe_{rf}}$, representing turbulence-dominated radial mixing
Specchia–Baldi wall-mixing model (Method 2)	Prandtl–Reynolds style scaling with geometric correction near wall, fit to data over wide $\mathrm{Re_p}$ and geometry ranges
Bauer–Schlünder wall-mixing correction (Method 3)	One-term function of local Reynolds number and mixing length, validated for moderate N and $\mathrm{Re_p}$
Winterberg–Tsotsas high-Pe limit (Method 4)	High–Peclet-number asymptotic expression where eddy conductivity grows with particle Reynolds number via a constant k

$$k_{\mathrm{rf}} = k_f\left(\frac{\mathbf{Pr}\bullet \mathbf{Re_p}}{k_\infty\left\{2-[1-(2/N)]^2\right\}}\right) \tag{27}$$

where k_∞ is an asymptotic mixing-limit constant (≈7 for spheres). Winterberg et al. (Winterberg et al., 2000) demonstrated agreement to within ± 10% across $\mathrm{Re_p} \approx 30 - 5000$ and $N \approx 3 - 12$.

2.2.2.3. Effective radial thermal conductivity k_r. The effective radial conductivity , k_r, Eq. (28) combines the effect of stagnant bed conductivity (k_{rs}) and the conductivity enhancement due to radial mixing of the fluid k_{rf} into a single effective thermal conductivity parameter (adapted from Specchia et al. (Specchia et al., 1980):

$$k_r = k_{rs} + k_{rf}. \tag{28}$$

2.2.2.4. Biot number Bi. The Biot number in packed-bed reactors quantifies the ratio of heat transfer through the wall to radial conduction through the bed of particles. Melanson & Dixon (Melanson and Dixon, 1985) originally derived a Biot-number formulation using experimental measurements of effective radial thermal conductivity and wall heat-transfer coefficients in stagnant annular fixed beds of spheres at low tube-to-particle diameter ratios. In that work, the Biot number was expressed in terms of the effective bed conductivity and separate wall Biot numbers for the solid and fluid phases, thereby capturing both solid and fluid resistances in the wall region under conduction-dominated conditions.

In the present study, we adopt the Melanson–Dixon Biot-number formulation as a generalized definition for fully packed cylindrical beds with flow, because it expresses Bi in terms of the same effective radial bed conductivity k_r, radial fluid conductivity k_{rf}, and wall heat-transfer submodels. This provides a consistent dimensionless measure of the competition between wall heat transfer and radial conduction for low d_t/d_p beds, even though our reactors are not stagnant annular systems.

According to (Melanson and Dixon, 1985);Bi can be defined as follows:

$$\mathbf{Bi} = \frac{4X}{1-X} \tag{29}$$

where the dimensionless grouping X blends the solid and fluid resistances in parallel with the total radial bed conductivity k_r (see Eq (55)):

$$X = 1/k_r \cdot \left(\frac{k_{rf}\mathbf{Bi}_f}{(\mathbf{Bi}_f+4)} + \frac{k_{rs}\mathbf{Bi}_s}{\mathbf{Bi}_s+4}\right) \tag{30}$$

The Biot number for solid, Bi_s, and fluid, Bi_f, are

$$\mathbf{Bi}_s = 2.41 + \left[0.156\left(\frac{d_t}{d_p}-1\right)\right]^2, \tag{31}$$

$$\mathbf{Bi}_f = \mathbf{Nu}_w^{\mathbf{Bi}}\frac{d_t}{2d_p}\frac{\mathbf{Pe}_{rf}}{\mathbf{Re_p Pr}}. \tag{32}$$

Here Nu_w is Nusselt number for tube wall (wall-fluid) heat transfer (called Nu_{wf} in the original reference), d_t is the tube diameter, and Pe_{rf} is radial fluid Peclet number shown in Eq. (33) and Eq. (34), respectively (Dixon (Dixon, 1988),

$$\mathbf{Nu}_w^{\mathbf{Bi}} = 0.523\left(1-\frac{d_p}{d_t}\mathbf{Pr}^{1/3}\bullet\mathbf{Re}^{0.738}\right) \tag{33}$$

$$\mathbf{Pe}_{rf} = \frac{\epsilon\cdot\tau}{\mathbf{Re_p}\cdot\mathbf{Pr}} + \frac{1}{\mathbf{Pe}_{rf\infty}}. \tag{34}$$

$Pe_{rf\infty} = 12$ is the limiting value of Pe as $Re_p \to \infty$, and τ is the bed tortuosity given by Maxwell (Maxwell, 1873) and defined in Eq. (35). Note that Eq. (33) is used for Nu_w^{Bi} when calculating Bi, even when another Nu_w method is selected (Section 2.2.3.1) for the calculation of overall heat transfer coefficient, U. Also,

$$\tau_b = 1.5 - 0.5\epsilon \tag{35}$$

For completeness, we also evaluated alternative Biot-number formulations, including the standard form, $Bi = \frac{h_w d_t}{2k_f}$. Across all DRM and CPOX cases considered in Section 3, changing the Bi definition (while keeping k_{rb}, k_{rf}, Nu_w, and Nu_{fs} correlations fixed) had a negligible impact on the predicted axial temperature and species profiles (e.g., changing the max or min temperature by just a few degrees K) compared to the variations induced by switching among different literature correlations for k_{rb}, k_{rf}, and Nu_w. Consequently, we retain the Melanson–Dixon formulation, Eq. (29–35) for all Biot-number calculations in this work, using it as a consistent, generalized dimensionless measure for low tube–to–particle diameter ratio packed beds rather than as a strict representation of their original stagnant annular configuration.

2.2.3. Convective heat transfer

2.2.3.1. Tube wall Nusselt number Nu_w. The wall Nusselt number, Nu_w, incorporates the convective heat transfer from the wall to the fluid, the conductive heat transfer through the bed (solid and fluid) near the wall, the convective heat transfer from fluid to the particles near the wall and the conductive heat transfer from the wall to the particles touching the wall. We evaluated three models for wall Nusselt number, Nu_w, summarized in Table 3. The detailed description of these three methods follows.

Nu_w Method 1: Extended Dixon-Cresswell wall-coupling model.

This correlation is adapted from Dixon and Cresswell (Dixon and Cresswell, 1979) and redefined by Dixon (Dixon, 1988). It treats the annular wall zone as a network of series/parallel resistances linking (i) gas–particle interfacial transfer, (ii) conduction through the packed layer, and (iii) contact paths to the tube wall. To capture these, the model introduces two composite dimensionless groups (Eqs. (36)-(39)):

$$N_s = \frac{\frac{1.5(1-\epsilon)}{(d_t/d_p)^2}}{\frac{k_{rb}}{k_f}\left[\frac{1}{Nu_{fs}} + \frac{0.1}{k_s/k_f}\right]} \tag{36}$$

$$\beta_s = \frac{(k_{rb}/k_f)}{8/N_s + (Bi_s + 4)/Bi_s} \tag{37}$$

$$N_f = \frac{\frac{1.5(1-\epsilon)}{(d_t/d_p)^2}}{\frac{Re_p \cdot Pr}{Pe_{rf}}\left[\frac{1}{Nu_{fs}} + \frac{0.1}{k_s/k_f}\right]} \tag{38}$$

Table 3
Correlations for wall Nusselt number, Nu_w evaluated in this work.

Nu_w Method Name	Key Idea / Origin
Extended Dixon–Cresswell wall-coupling model (Method 1)	Detailed series–parallel resistance model for wall region, distinguishing high- and low-Re_p regimes, tuned for laminar–transitional flow in packed beds
Dixon 2011 blended convection–conduction correlation (Method 2)	Single algebraic correlation that blends turbulent convection, mixing-cell, and pure wall-conduction limits via a harmonic mean
Two-term Martin–Nilles correlation (Method 3)	Compact two-term fit combining wall-conduction and Dittus–Boelert-type convection, based on a large experimental database

$$\beta_f = \frac{Re \cdot Pr / Pe_{rf}}{8/N_f + (Bi_f + 4)/Bi_f} \tag{39}$$

Here, ϵ is the bed porosity, k_f and k_s are the pure conductivities of fluid and solid material, Nu_{fs} the local fluid–solid Nusselt number (Section 2.2.1.5), Bi_s and Bi_f the solid- and fluid-phase wall Biot numbers, and Pe_{rf} the radial thermal Peclet number of the fluid. Nu_{fs} is the Nusselt number for fluid–solid heat transfer. Various correlations were evaluated for Nu_{fs}, as will be discussed in Section 2.2.3.2. However, in the end the correlation of Wakao–Kaguei (Wakao and Kagei, 1982), Eq. (52), is selected for all results where Nu_w Method 1 (Dixon-Cresswell) is used when calculating results presented in Section 3.

The final expression for the wall Nusselt number depends on flow regime:

For high-velocity regime i.e., $Re \geq 50$,

$$Nu_w = \frac{8\beta_s}{d_t/d_p} + Nu_{wf}\left(1 + \frac{\beta_s Pe_{rf}}{Re_p \bullet Pr}\right), \tag{40}$$

where, Nu_{wf} is an auxiliary wall-layer Nusselt number evaluated with wall-layer properties. Turbulent dispersion dominates because, at $Re_p \geq 50$ the wall Nusselt number exceeds the 'conduction limit' set by the static wall–layer pathways (those captured by the β_s terms and solid/fluid conductivity ratios), so the $\frac{\beta_s Pe_{rf}}{Re_p \bullet Pr}$ term represents the main additional, velocity–dependent enhancement due to eddy mixing in the wall region rather than simple molecular conduction.

For low-velocity regime i.e., $Re_p < 50$,

$$Nu_w = \frac{8\beta_f}{d_t/d_p} + \frac{2Bi_s(k_{rb}/k_f)(d_p/d_t)(1+\beta_f)}{k_{rb}/k_f}. \tag{41}$$

If wall-layer conduction is rate-controlling, Eq. (41) reverts to a conduction-dominated form governed by β_f. Dixon's experimental data ($d_p/d_t = 5 - 12$, $Re_p = 100 - 1000$) showed that the model predicts within $\pm$ 10% for non-metallic packings and remains qualitatively accurate for metallic spheres (Dixon, 1988; Dixon and Cresswell, 1979).

Nu_w Method 2: Blended convection–conduction correlation by Dixon (Dixon, 2012).

This shortcut expression merges three limiting behaviours into a single algebraic form so that the same formula remains valid from laminar through highly turbulent flow and from large to narrow tubes. The turbulent-convection limit is represented by Eq. (42)

$$Nu_w^* = 0.3 Pr^{1/3} \bullet Re_p^{3/4} \tag{42}$$

the intermediate "mixing–cell'' limit by Eq. (43)

$$Nu_m = 0.054 Pr \bullet Re_p \tag{43}$$

and the pure wall-conduction term by Eq. (44)

$$Nu_{w0} = \left(1.3 + \frac{5}{d_t/d_p}\right)\frac{k_{rb}}{k_f}. \tag{44}$$

Pr is the Prandtl number of the fluid. The three contributions are combined through harmonic mean (Eq. (45))

$$Nu_w = Nu_{w0} + \frac{1}{\frac{1}{Nu_w^*} + \frac{1}{Nu_m}}. \tag{45}$$

Dixon (Dixon, 2012) showed that, for non-metallic beds in the ranges $N = d_t/d_p \approx 3 - 12$ and $\epsilon \approx 0.35 - 0.45$, the correlation reproduces measured wall Nusselt numbers to within $\pm$ 12%.

Nu_w Method 3: Two-term Martin-Nilles correlation

For quick engineering estimates a still more compact expression, distilled from the large experimental data-base of Martin & Nilles

(Martin and Nilles, 1993), exists (Eq. (46)):

$$\mathbf{Nu}_w = \left(1.3 + \frac{5}{N}\right)\frac{k_{rb}}{k_f} + 0.19\mathbf{Pr}^{1/3}\mathbf{Re}_p^{3/4} \tag{46}$$

where the first term represents the wall-conduction limit and the second is a Dittus–Boelter-type convection term that dominates for $Re_p \geq 50$. Martin & Nilles (Martin and Nilles, 1993) validated the form for spherical and ring packings in windows $N \approx 3 - 25$, $30 \leq Re_p \leq 5000$, and $\epsilon \approx 0.35 - 0.45$ to within ± 12%.

2.2.3.2. Fluid-solid Nusselt number Nu_{fs}. The heat transfer between fluid and particle surfaces inside the bed is controlled via the fluid–solid heat transfer coefficient h_{fs}. Specifically, it is possible to model heat transfer from the bulk gas to each catalyst pellet through the fluid boundary layer that envelops the particles (Eq. (8)). The interphase coefficient is evaluated from a Nusselt number, as shown in Eq. (47).

$$h_{fs} = \frac{\mathbf{Nu}_{fs} \bullet k_f}{d_p} \tag{47}$$

The three methods tested to calculate Nu_{fs} are summarized in Table 4 and discussed further below.

Nu_{fs} Method 1: Gnielinski single-sphere correlation with porosity factor.

For flow around an isolated sphere, Gnielinski (Gnielinski, 2010) splits the Nusselt number into laminar (Eq. (48)) and turbulent (Eq. (49)) contributions:

$$\mathrm{Nu}_{\mathrm{lam}} = 0.664 \cdot \mathrm{Pr}^{\frac{1}{3}} \bullet \mathrm{Re}_{\epsilon}^{\frac{1}{2}} \tag{48}$$

$$\mathbf{Nu}_{\mathrm{turb}} = \frac{0.037 \cdot \boldsymbol{Pr} \bullet \mathbf{Re}_{\epsilon}^{0.8}}{1 + \left(2.443 \cdot \mathbf{Re}_{\epsilon}^{-0.1}\left(\mathbf{Pr}^{2/3} - 1\right)\right)} \tag{49}$$

with the void corrected $Re_\epsilon = Re/\epsilon$. The two regimes are combined as following (Eq. (50)):

$$\mathbf{Nu}_{\mathrm{sphere}} = 2.0 + \sqrt{\mathbf{Nu}_{\mathrm{lam}}^2 + \mathbf{Nu}_{\mathrm{turb}}^2} \tag{50}$$

For a bed of spheres Gnielinski (Gnielinski, 2010) proposes a linear porosity correction that enhances the surface-averaged coefficient as the void fraction decreases:

$$\mathbf{Nu}_{fs} = (1 + 1.5(1 - \epsilon))\mathbf{Nu}_{\mathrm{sphere}} \tag{51}$$

Equations (48)–(51) were validated for air and water flowing over beds of non-conductive glass spheres in the ranges $\epsilon \approx 0.35 - 0.45$, $Pr \approx 1 - 100$, and $Re_\epsilon \approx 20 - 6000$ with a reported accuracy of ± 10% (Gnielinski, 2010).

Nu_{fs} Method 2: Wakao & Kaguei packed-bed correlation

For rapid engineering estimates the correlation of Wakao–Kaguei (Wakao and Kagei, 1982) is widely used, which expresses the particle-based Nusselt number as a single power-law, shown in Eq. (52):

$$\mathbf{Nu}_{fs} = 2.0 + 1.1\left(\mathbf{Pr}^{1/3} \bullet \boldsymbol{Re}_p^{0.6}\right). \tag{52}$$

Wakao & Kaguei (Wakao and Kagei, 1982) validated the correlation for beds of spheres and cylinders over $Re_p \approx 15 - 10{,}000$ and $Pr \approx 0.7 - 7$, reporting a ± 10% scatter against 250 literature data sets.

Nu_{fs} Method 3: KTA correlation

KTA (Nuclear Safety Standards, 1983) provided a compact, two-term fit that spans both laminar and fully turbulent flow through tightly specified porosity windows. Expressed on a particle basis (Eq. (53)),

$$\mathbf{Nu}_{fs} = \frac{1.27 \cdot \mathbf{Pr}^{1/3} \cdot \mathbf{Re}^{0.36}}{\epsilon^{1.18}} + \frac{0.033 \cdot \mathbf{Pr}^{1/2} \cdot \boldsymbol{Re}_p^{0.86}}{\epsilon^{1.07}} \tag{53}$$

covers $Re_p \approx 100 - 100000$, $\epsilon \approx 0.35 - 0.45$, $Pr \approx 0.7 - 1$, and $N > 20$, reporting a ± 20% deviation.

*2.2.4. Overall heat transfer coefficient **U***

The overall heat transfer coefficient U quantifies radial heat transfer within packed-bed reactors by combining resistances due to conduction through the reactor wall, heat transfer within the packed bed itself, and external convective resistance. Using the improved equation proposed by Dixon (Dixon, 1996); U is written as

$$\frac{1}{\boldsymbol{U}} = \frac{1}{\boldsymbol{h_w}} + \frac{\boldsymbol{d_t}}{6\boldsymbol{k_r}} \bullet \frac{\mathbf{Bi} + 3}{\mathbf{Bi} + 4} + \frac{\boldsymbol{d_t}}{\boldsymbol{d_{l_m}}} \bullet \frac{\boldsymbol{x_w}}{\boldsymbol{k_w}} + \frac{\boldsymbol{d_t}}{\boldsymbol{d_o}} \bullet \frac{1}{\boldsymbol{h_o}}\left[\frac{\boldsymbol{m}^2 \bullet \boldsymbol{K}}{\boldsymbol{W}}\right]. \tag{54}$$

The four terms on the right hand side reflect the heat transfer between inner tube wall and fluid, the heat transfer through the bed (combination of fluid and solid), the heat transfer through the tube wall and the heat transfer at the outer surface of the tube.

d_t and d_o are, respectively, the tube-inside and tube-outside diameters, d_{l_m} is the logarithmic-mean diameter, k_w is the conductivity of tube wall, x_w the tube wall thickness, h_w is the heat transfer coefficient at inner tube wall, and h_o is the external heat transfer coefficient between outer tube wall and surroundings. The first two terms on the right hand side reflect the heat transfer between inner tube wall and bed, the heat transfer through the bed (combination of fluid and solid). The second two terms describe the heat transfer through the tube wall and the heat transfer at the outer surface of the tube. Both are omitted here as we assumed an infinitesimally thin, perfectly conducting wall ($x_w = 0$) and no resistance at outer wall ($h_o = \infty$).

The resistances-in-series of Eq. (54) shows that the U is the connection point of the two hierarchies or branches of sub-correlations, colored in blue and green in Fig. 1. On left side we can identify the *wall branch* (in blue). Here, the wall heat transfer coefficient h_w, models wall-side phenomena via Eq. (55), where the wall Nusselt number Nu_w is calculated from one of the several empirical expressions (Methods 1–3 in Section 2.2.3.1). The wall heat transfer coefficient h_w is related to the wall Nusselt number (Nu_w) by:

$$\boldsymbol{h_w} = \frac{\mathbf{Nu}_w \boldsymbol{k_f}}{\boldsymbol{d_p}}. \tag{55}$$

2.2.5. Convective mass transfer

2.2.5.1. Fluid-solid mass transfer coefficient k_{fs}. Because interphase heat and mass transport in packed beds follow analogous boundary-layer physics, fluid–solid mass transfer coefficient of the i^{th} species, $k_{fs,i}$ (Eq. (7)) (also simply written as k_{fs} in this paper)can be estimated by replacing the thermal dimensionless groups in the chosen heat-transfer correlation (Eqs. (51)-(53)) with their mass-transfer counterparts (Incropera and David, 1996):

$$\mathbf{Nu}_{fs} \rightarrow \mathbf{Sh}_{fs}, \mathbf{Pr} \rightarrow \mathbf{Sc} \tag{56}$$

The resulting Sherwood and Schmidt numbers are defined by:

Table 4
Correlations for radial fluid–solid Nusselt number, Nu_{fs}, evaluated in this work.

Method Name	Key Idea / Origin
Gnielinski single-sphere with porosity factor (Method 1)	Combines laminar and turbulent sphere correlations, then applies a linear porosity correction for beds of spheres
Wakao–Kaguei packed-bed correlation (Method 2)	Single power-law for particle Nusselt number vs. particle Reynolds and Prandtl numbers, widely used for packed beds
KTA (1983) correlation (Method 3)	Two-term fit spanning laminar to fully turbulent regimes for specified porosity and Re windows

Table 5
Grid parameters.

Grid number	N = D/d_P	Particle diameter [mm]	Number of particles	total count of cells	count of fluid cells	count of solid cells	Count of reactive surface cells
1	1.1	23.00	23	1,744,582	1,213,984	530,598	120,271
2	2.0	12.70	86	2,333,930	1,559,544	774,386	217,810
3	7.0	3.62	6000	23,704,492	14,109,467	9,595,025	4,004,587

Table 6
Bed parameters.

Grid number	N = D/d_P	Particle diameter [mm]	Number of particles	Averaged porosity [-]	Specific particles surface [m^2/m^3]
1	1.1	23.00	23	0.453	162.15
2	2.0	12.70	86	0.644	46.21
3	7.0	3.62	6000	0.416	261.97

$$\mathbf{Sh}_{fs,i} = \frac{d_p k_{fs,i}}{D_{\mathrm{eff,i}}} \tag{57}$$

$$\mathbf{Sc}_i = \frac{\mu}{\rho D_{\mathrm{eff},i}} \tag{58}$$

where μ is the fluid mixture viscosity, and $D_{\mathrm{eff},i}$ is effective mass diffusivity.

2.2.6. Solver PBR

The 1D packed-bed reactor code PBR (Packed Bed Reactor) (Mokashi et al., 2024; Shirsath et al., 2023) is written in FORTRAN and part of the DETCHEM^{TM} software package (Deutschmann et al., 2014). The system of ordinary differential equations is solved numerically along the reactor axis with inlet and initial conditions (provided in Tables 7 and 8), using the differential–algebraic solver LIMEX (Deuflhard et al., 1987). The distance between axial nodes is determined automatically by the LIMEX algorithm, based on settings of relative and absolute tolerances, such that in regions of large gradients the distance between axial nodes decreases. Properties such as density, viscosity, specific heat, molar weight, velocity, pressure, surface reaction rates, and heat and mass transfer coefficients were updated after each integration step. Further information about acquiring PBR can be obtained from omegadot Software & Consulting GmbH (www.omegadot.software).

2.3. 3D modeling of packed bed reactors

In the following sections, the numerical setup for the 3D modeling is described, including the description of the solver DUO, the approach used for meshing and an overview of boundary conditions applied.

2.3.1. Solver DUO

OpenFOAM (OpenFOAM, , 2017) is an open-source finite volume computational fluid dynamics (CFD) software package. Presently, OpenFOAM is not natively capable of modeling systems involving surface chemistry. Therefore, the tool DUO (Hettel et al., 2018; Hettel et al., 2015) was used for the calculations. **DUO** stands for the coupling of the two computer codes **D**ETCHEM^{TM} **U**nd (German for 'and') **O**penFOAM and is a synonym for the joint utilization of these two programs. DETCHEM^{TM} (Deutschmann et al., 2014) is a commercially available package of tools specifically designed for the modeling and simulation of reacting flows based on elementary step mechanisms, e. g. for catalysis, materials synthesis and fuel cells. DUO is a commercial application that combines the advantages of the two programs by enhancing the functionality of OpenFOAM with respect to the calculation of heterogeneous surface reactions. Further information about acquiring DETCHEM^{TM} and DUO can be obtained from omegadot Software & Consulting GmbH (www.omegadot.software).

The mass and energy balance equations associated with DETCHEM^{TM} DUO are described in (Benzinger et al., 2019), while the cell agglomeration and In-Situ Adaptive Tabulation (ISAT) approaches used for the PRCFD calculations are discussed in Daymo et al. (Daymo et al., 2022).

Table 7
Inlet / outlet boundary conditions for CPOX cases.

Quantity	Unit	inlet	outlet
N_2	vol-%	80.00	zero grad.
CH_4	vol-%	13.33	zero grad.
O_2	vol-%	6.67	zero grad.
T	K	973	zero grad.
U	m/s	see table 9	zero grad.
p (DUO)	Pa	zero gradient	101,325
p (PBR)	Pa	101,325	none

Table 8
Inlet / outlet boundary conditions for DRM cases.

Quantity	Unit	inlet	outlet
CH4	vol-%	50.00	zero grad.
CO_2	vol-%	50.00	zero grad.
T	K	973	zero grad.
U	m/s	see table 9	zero grad.
p (DUO)	Pa	zero gradient	101,325
p (PBR)	Pa	101,325	none

2.3.2. Bed generation, meshing, porosity analysis

The calculation domain consists of a tube with a length of L = 110 cm and a tube diameter of $d_t = 2.54$ cm. Inside the tube a packed bed region being 50 cm long is positioned 10 cm downstream from the inlet.

The packed beds were generated synthetically using the Rigid Body approach implemented in the open-source software Blender V2.79. After the particles are settled and shrunk by 2% to prevent particles from touching, the packed bed geometries were exported as STL files. A polyhedral computational mesh for the fluid and solid domains was generated using the meshing algorithm of the commercial CFD code Siemens Simcenter STAR-CCM + based on the STL files. The mesh was written out in a format to be readable from the CFD software ANSYS FLUENT. From there the mesh could be saved in ASCII format. Conversion to OpenFOAM was accomplished with the OpenFOAM tool fluent3DMeshToFoam. The OpenFOAM utility splitMeshRegions was used to create the fluid and solid (pellet) regions.

Three different meshes for three different particle diameters d_P and therefore also for three different ratios of diameters of tube and particles (d_t/d_p = N = 1.1/2/7) were generated. The number of particles, the cell counts and the total number of reactive surface cells of particles can be found in Table 5. Sketches of the corresponding PRCFD beds are shown in Fig. 2. The top of Fig. 2 shows the overall geometry for the three values of N, serving as a schematic of the tube and beds being modeled by 1D and 3D methods. The interior of the particles in Fig. 2 reveals the

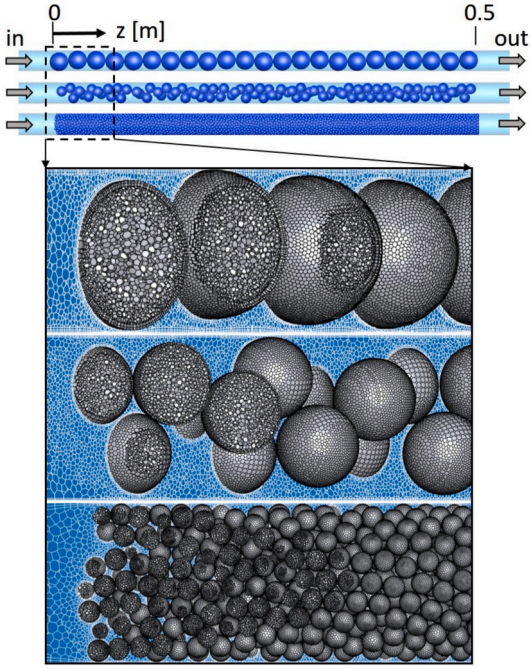

Fig. 2. Sketch of beds and cutout of polyhedral grids. From top to bottom: N = 1.1/2.0/7.0.

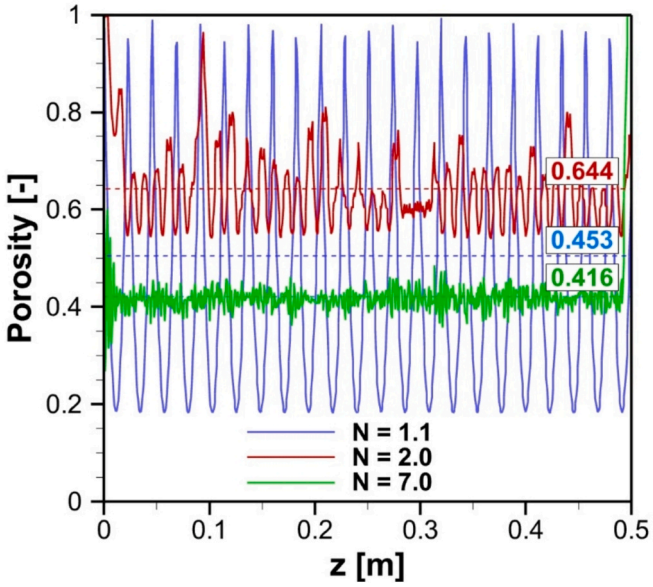

Fig. 3. Local porosities over bed length for the three beds. The dashed lines and the related numbers depict the volume averaged porosities.

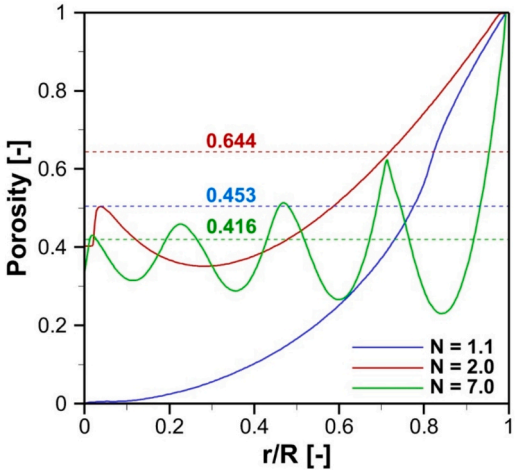

Fig. 4. Porosities over radius for the three beds. The dashed lines and the related numbers depict the volume averaged porosity.

presence of grid cells. This interior is modeled as a solid region where only heat transfer occurs. There is no diffusion inside the pellets for the present work, such as that described by Dixon 2010. This decision was made because the primary objective of this study is to compare 1D and 3D methods for describing external heat and mass transfer, which could be confounded by the additional multiphysics of internal pore diffusion. This said, other studies have shown good comparison between 3D and/or 1D and 2D (Dixon, 2021a; Dixon, 2017) and 3D and 2D (Daymo and Hettel, 2026) with pore diffusion models enabled, albeit with fewer correlations tested in the pseudo-continuum model calculations.

In Table 6 typical parameters of the three beds are shown. The averaged porosities for N = 1.1 and 7.0 are roughly the same. However, the bed with N = 7.0 shows a significantly larger specific particle surface area compared to the bed with N = 1. The bed with N = 2.0 is special compared to the two other ones. Here, the porosity is quite large and the particle surface area is quite small. This is because for this particle size not more than two particles can be beneath each other at any axial position. This leads to regions in the bed where the space between particles is large and therefore the overall surface per volume is relatively small (see Figs. 2 and 3).

The porosities over axial coordinate z along the three beds are shown in Fig. 3. The bed with the largest particles (blue line, N = 1.1) exhibits 23 wiggles. Each wiggle represents a particle where the porosity changes between a minimum value of ca. 0.2 (particles overlap slightly near contact point) and a maximum value which is around 0.95. The minimum value of each wiggle is at an axial position where a particle touches the tube wall. The volume averaged porosity of this bed is 0.453. Meanwhile, the bed with (N = 2) shows wiggles with a smaller amplitude. The amplitude is not constant, and the number of wiggles is smaller than the number of particles. The averaged porosity of this bed is 0.644. The bed with the smallest particles (green line, N = 7) exhibits a relatively constant porosity along the bed which fluctuates with small amplitude around the average value of 0.416.

The porosities over normalized radial position r/R of the beds are shown in Fig. 4. At the wall of the tube the porosity is one for all cases. The bed with the smallest particles (green line, N = 7) shows the well-known behavior of an oscillating porosity whereas the amplitude of oscillation reduces towards the center of the bed. Starting at wall, the bed with N = 2 (red line), porosity decreases to a minimum value near r/R = 0.3. Then, porosity increases and exhibits a local maximum near r/R = 0.025. The porosity at the centerline for N = 2 is 0.4. The porosity for the bed with the largest particles (blue line, N = 1.1) exhibits a monotonously decreasing curve with value zero at the center of the bed.

2.3.3. Boundary conditions and parameters

Inlet and outlet boundary conditions for the CPOX and DRM cases are given in Tables 7 and 8, respectively.

A no-slip condition is imposed at the walls, while pressure and species are set to zero gradient at the walls. The zero gradient condition was also set for all quantities at the outlet area. As usual for CFD (DUO), the pressure was defined at the outlet and zero gradient was applied at the inlet. As PBR solves a set of ordinary differential equations, pressure is set to a fixed value at the inlet. Nonetheless, pressure loss is for all cases negligible, with effectively no effect on density, velocity, and kinetics.

Region coupled boundary conditions, which allow heat flux between

fluid and solids, were applied at all particle–fluid interfaces. The solid thermal conductivity of the particles, λ, was set to 1 W/(m·K) for all cases. However, there is no fluid inside the particles (e.g., no internal resistances), and no washcoat model is applied at the surface. Such details are unnecessary for this study since we aim to compare 1D and 3D results without the additional complication of pore diffusion resistances. Likewise, a radiation model is not utilized because of the same rationale.

The typical particle Reynolds number Re_p for the system is defined using the velocity at the inlet of the empty tube, the particle diameter d_p and the kinematic viscosity ν_{in} of the mixture at the inlet (Eq. (59))

$$\mathbf{Re}_p = \frac{\boldsymbol{u}_{in} \bullet \boldsymbol{d}_p}{\boldsymbol{\nu}_{in}} \tag{59}$$

Four different particle Reynolds numbers Re_p have been compared (all references to Reynolds numbers in this paper are particle Reynolds numbers, unless otherwise specified). The corresponding inlet velocities can be found in Table 9.

Two temperature boundary conditions were applied. For the first set of calculations, an adiabatic tube wall (no heat flux) was evaluated. For the second set of calculations (non-adiabatic, non-isothermal), the wall temperature was set to 973 K, which is the same as the inlet temperature of the mixture.

The values for $F_{cat/geo}$ can be found in Table 10. The values for N = 1.1 and 2 are the same as in (Daymo et al., 2022). For N = 7 the values of $F_{cat/geo}$ were reduced. This is due to the large value of the bed surface area to volume ratio, which leads to full conversion within a very short distance inside the bed unless $F_{cat/geo}$ is substantially reduced.

It is further noted that for all calculations, 2nd order discretization schemes were utilized for space. To obtain the steady state solution we used a transient scheme with first order and a large time step. Ideal gas and kinetic theory were assumed for applicable gas phase properties.

Some the calculations for larger velocities were performed with and without the k-Omega SST turbulence model enabled. Since there was no difference in the result, all subsequent calculations were done assuming laminar flow.

3. Results

In this section comparisons of 1D and 3D calculations are discussed for adiabatic conditions (Section 3.1) and non-adiabatic conditions (Section 3.2) each for two chemistries. However, before a comparison of quantities along the axis of the tube can be performed, the results from the PRCFD calculations must be postpocessed.

In particular, comparisons of 1D and 3D model results require radially mass flow averaged quantities along the length of the packed bed. It is noted that the radially mass flow averaged quantities differ from same quantities found along the symmetry axis of the tube for PRCFD results. The ratio of the reactive pellet surface area to reactor volume is larger at the center than towards the adiabatic wall. Furthermore, the porosity along symmetry axis is smaller than the radially averaged value (see Fig. 4).

This effect can be seen in Fig. 5, where the principal differences between centerline and radially mass flow averaged quantities are clearly visible for CH_4 and H_2 (CPOX case with N = 2). As shown, the local conversion of CH_4 along the centerline (blue dots) is larger than the averaged conversion (blue line). The values on the centerline also seem

Table 9
Particle Reynolds numbers and inlet velocities u_{in}.

Reynolds number	N = 1.1 [m/s]	N = 2 [m/s]	N = 7 [m/s]
29	0.11	0.20	0.70
145	0.55	1.00	3.50
290	1.10	2.00	–
1450	5.50	10.00	–

Table 10
Values of $F_{cat/geo}$.

Reaction	N = 1.1 [-]	N = 2 [-]	N = 7 [-]
CPOX	5.64	5.64	1.00
DRM	90.00	90.00	5.64

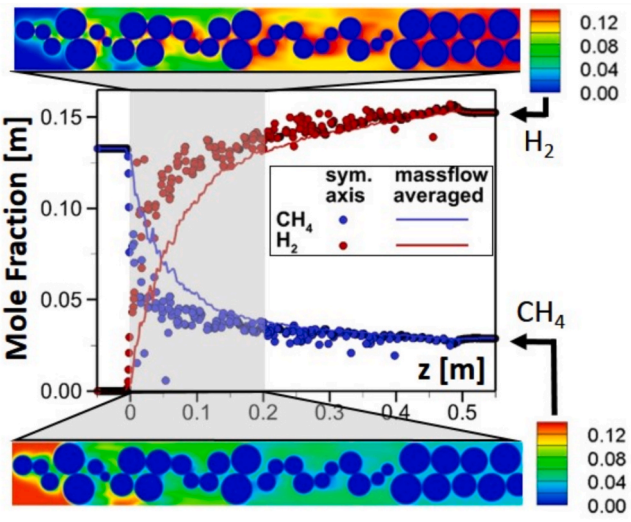

Fig. 5. Species for CPOX case: N = 2, Re_p = 290, adiabatic wall. Bed is in region 0 m < z < 0.5 m). Upper isoplot: slice of H_2 mole fraction through the centerline of the reactor (0.01 m < z < 0.1 m). Lower isoplot: slice of CH_4 mole fraction through the centerline of the reactor (0.01 m < z < 0.1 m). Line plot: concentration results along the symmetry axis (dots) as well as radially averaged results (lines).

to show a chaotic behavior, due the presence of particles where there is no flow. This is because two neighboring positions on the axis may exhibit very different concentration values dependent on the position in the flow field and the distance to the next particle surface. Inverse characteristics as for CH_4 can be seen for the concentration of H_2. Here the values along the centerline (red dots) are larger than the averaged values (red line).

Fig. 6 shows an analysis for the temperature field of a DRM case for N = 1.1. The two upper isoplots display the temperature field inside

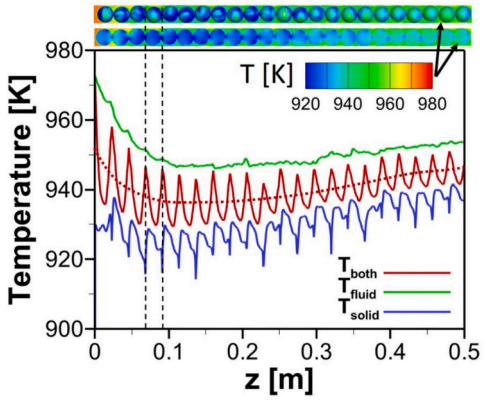

Fig. 6. Temperature profiles for DRM case: N = 1, Re_p = 1450, wall temperature 973 K, in the region of bed (0 m < z < 0.5 m). Isoplots: slices of gas phase temperature through the centerline of the reactor. Upper plot is with temperature on surface of particles, lower plot is with temperature inside sliced particles. Line plot: cross-sectional averaged temperatures of fluid, solid and both phases together and regression curve (dotted line) for T_{both}.

fluid and solid domains. As the DRM reaction is endothermic, the temperature drops in the first 0.1 m of the bed, where most of the conversion occurs. Downstream the overall temperature increases due to heat flux from wall into gas and from the gas into particles. As particles are shrunk by 2% (see 2.3.2) no particles touch the wall directly and the wall temperature is fixed at 973 K. The green line shows the mass flow averaged temperature of the mixture, which is relatively smooth along the reactor. The blue line depicts the area averaged temperature inside of the solid particles. It can be seen that the temperature inside the solids is typically larger at the front side compared to the rear side. The solid red line (T_{both}) shows the average temperature of both phases (fluid and solid) combined. To calculate the average temperature, fluid and solid phase temperatures are summed and weighted with local porosity at every z-position. It is observed that T_{both} exhibits strong wiggles, with the maxima are positioned between two particles. Here, solely hot gas can be found (local porosity is zero). This behavior is marked at two positions in Fig. 5 by vertical dashed lines. It is noted that for N = 2 and 7, the wiggles in T_{both} are much smaller. To help compare 3D and 1D results (which have no temperature wiggles since porosity is constant), a regressed average (T_{both}) temperature (the dotted red line in Fig. 6) is produced, which eliminates the wiggles in the average temperature. This approach holds also for all graphs shown later.

3.1. Adiabatic conditions

Simulations under adiabatic conditions were performed to evaluate the intrinsic fidelity of the 1D model in capturing reaction kinetics and species transport without the complexity of external heat transfer. Also, the effects of external and mass transfer resistances were evaluated. The study spanned tube-to-particle diameter ratio (N = 1.1, 2, 7) and particle Reynolds numbers (Re_p = 29, 145, 290 and 1450), covering the regime typical of industrial fixed-bed reactors.

No wall heat transfer correlations, including wall or intra-bed (radial) thermal conductivity, were applied to the 1D case, since these correlations feed into the overall heat transfer coefficient, U (Fig. 1), and U (in $[W/m^2/K]$) is zero in Eq. (8) under adiabatic conditions. This setup isolates transport and reaction effects to assess 1D–3D consistency prior to introducing wall heat-transfer models.

With respect to external heat and mass transfer resistances, as will be discussed below, adiabatic conditions were also used to determine the effect of external heat and mass transfer resistances, (i.e., the transport of heat and mass from bulk phase, across the boundary layer, to the particle surface). A series of tests were done for every bed (N = 1, N = 2, and N = 7), across all evaluated Re_p numbers, with all three correlations described in Section 2.2.3.3. For each bed (N value), flow rate, and external heat and mass transfer correlation, species and temperature profiles were compared for cases with heat and mass transfer resistances both enabled (HT = on, MT = on), heat and mass transfer resistances both disabled (HT = off, MT = off), heat transfer resistance enabled but mass transfer resistance disabled (HT = on, MT = off), and heat transfer resistance disabled but mass transfer resistance enabled (HT = off, MT = on). When HT = on, MT = on, the same method for the Nusselt and Sherwood numbers was selected (i.e., if Nu Method 2 was tested, then Sh Method 2 was selected as well).

Note that in the PRCFD case, even though the walls were adiabatic, conduction within the packed bed still occurred. Also, PBR does not model axial conduction effects.

3.1.1. Dry methane reforming (DRM)

Initial testing with external heat and mass transfer resistances, regardless of which of three correlations discussed in Section 2.2.3.3 was selected, showed that for DRM with the N = 7 bed the fluid and solid temperatures were identical (along with the species profiles) irrespective of whether external heat transfer resistances were on or off, or external mass transfer resistances were on or off. The reason is that for this bed with smallest particles the specific particles surface (surface area per bed volume) is much larger than for the two other beds (see Table 6.)

The characteristics were different for both the beds N = 1 and N = 2. An example is shown in Fig. 7 for N = 2, Re_p = 290 (u = 2 m/s). The left columns show the comparison of temperatures. Whenever the solid energy balance is disabled in the 1D model (HT = off in Fig. 7 left, plots 1 and 2) the fluid and solid temperatures are in equilibrium (i.e., $T_{solid} = T_{gas}$). In these cases the temperature fits best to the mixed temperature (averaged solid and fluid temperature) from PRCFD at front of the bed. Towards the end the 1D temperature is closer to that of the solid temperature in the 3D results.

For the cases where two energy balances are solved in 1D (HT = on in Fig. 7 left, plots 3 and 4), the solid and fluid temperatures fit quite well to those of the 3D model. Notably, the temperature of the solid decreases relative to the fluid due to the endothermic reaction occuring at the particle surface. The difference between temperature of solid and fluid phase is largest at the entrance to the bed (where the reaction rate is fastest) and decreases downstream (where the reaction rate is lower but the wall continues to heat up the bed). This shows that, if needed, the 1D model is able to predict both temperatures (for solid and fluid) separately.

For N = 1 and N = 2, *species profiles* were nearly identical the regardless of whether external heat and/or mass transfer resistances were enabled or disabled (see Fig. 7 right column).

As a result of these tests with external heat and mass transfer resistances, all further adiabatic and non-adiabatic, non-isothermal tests with DRM presented below assumed that external heat and mass transfer resistances can be ignored.

Fig. 8 shows the comparison of mass-flow averaged 3D PRCFD results (symbols) and results of the 1D model (lines) for DRM chemistry for all three beds for the conditions HT = off and MT = off. In first row the molar fractions of gas species CH_4 and H_2 are compared, in second row the temperature. In both rows the ratio N increases from left to right (smaller particles). Under adiabatic conditions, the endothermic nature of DRM results in a notable temperature drop across the reactor length, with good agreement between the 1D (lines) and 3D (markers) results. At lower Re_p numbers (Re_p = 29, 145), the temperature decline is more pronounced owing to the extended residence times, which facilitats greater heat consumption by the reaction. Conversely, at higher Re_p numbers (Re_p = 290 and 1450), the reduced residence times limit the reaction extent, resulting in smaller temperature drops. CH_4 conversion decreases monotonically as the Re_p number rises, whereas the H_2 mole fraction becomes largest at low Re_p where reaction completion is greatest. When N = 1.1, the small spacing between particles enhances external mass transfer and produces slightly higher conversion than at larger N. A comparison between the 1D and 3D simulations shows good agreement. Deviation in CH_4 and H_2 profile remains below 2% once Re $\geq$ 290. Furthermore, small temperature offsets, below 4%, appear only for N = 1.1 at Re_p = 145 and below, where radial gradients, that a one-dimensional framework cannot resolve, become significant.

3.1.2. Catalytic partial oxidation (CPOX)

Initial testing with external heat and mass transfer resistances, regardless of which of three correlations discussed in Section 2.2.3.3 was selected, showed that for CPOX with the N = 7 bed, fluid and solid temperatures were identical (along with the species profiles). This observation with the N = 7 bed did not depend on whether external heat transfer resistances were on or off, or external mass transfer resistances were on or off. The reason is that for this bed with smallest particles the specific particles surface (surface area per bed volume) is largest (see Table 6.).

As previously discussed for DRM, for CPOX the characteristics were also different for the beds N = 1 and N = 2. A typical example is shown in Fig. 9 for N = 2, Re_p = 290 (u = 2 m/s). The comparison of temperatures is in the left column. The characteristics of the temperature in the PRCFD

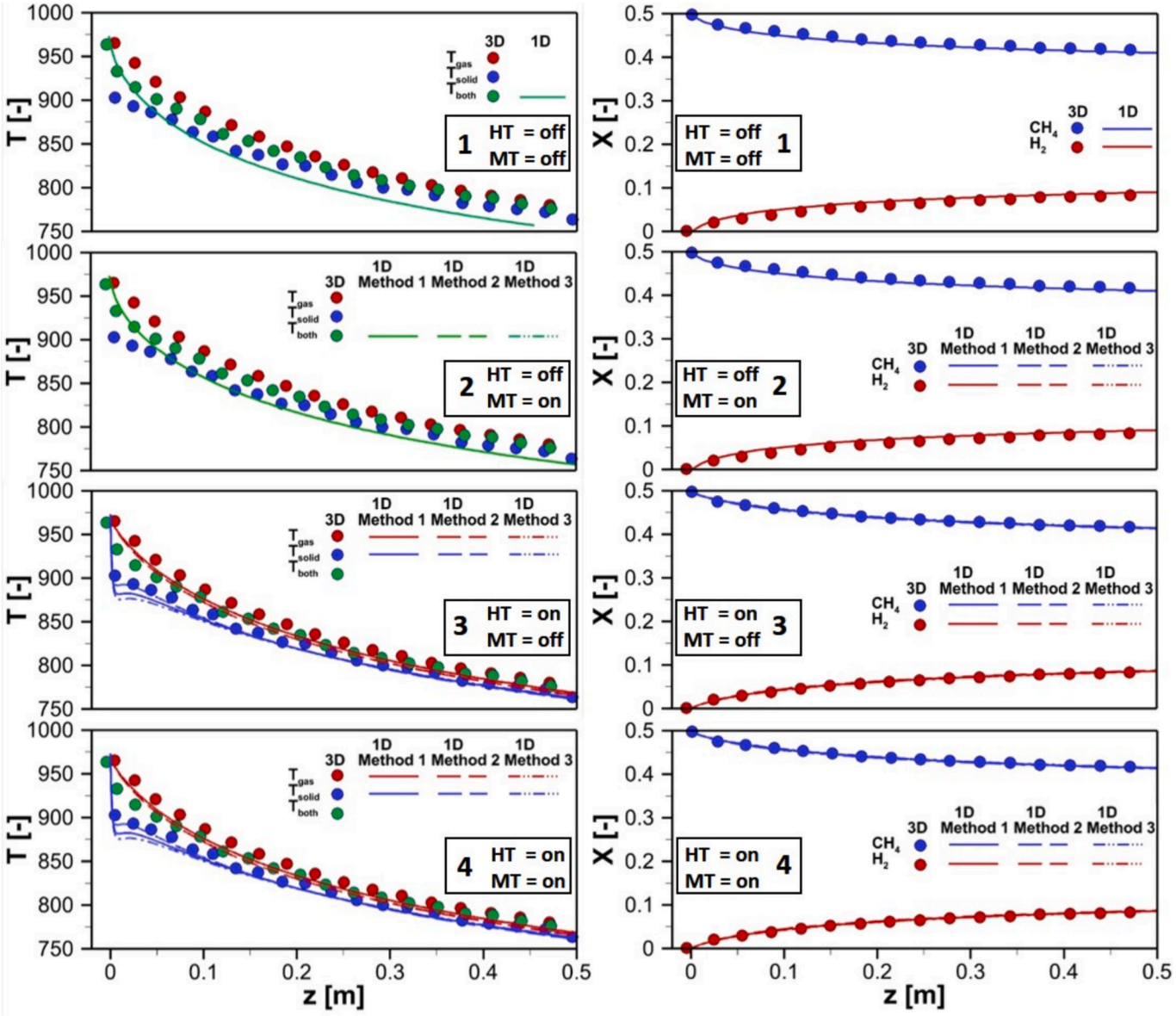

Fig. 7. Adiabatic DRM results for N = 2, Re_p = 290 (temperature left, species right). HT = on/HT = off refers to whether external heat transfer resistance is enabled, and MT = on/MT = off denotes whether external mass transfer resistances are enabled. Method number refers to the Nu_{fs} Method (correlation) in Section 2.2.3.2.

follows the typical behaviour indicating two different zones (e.g. Hettel et al. (Hettel et al., 2018; Hettel et al., 2015). In the first zone the oxygen is consumed leading to an increase of temperature. Simultaneously occurring steam reforming reactions lead to the formation of hydrogen and carbon monoxide via the reaction of methane with water. In the the second zone, the endothermic steam reforming reaction is predominant after all oxygen has been consumed, causing a decrease in temperature, further consumption of methane, as well as formation of hydrogen and carbon monoxide.

We now focus on the 1D results. In the two cases with MT = off (Fig. 9 left, plots 1 and 3) there is a distinct peak in temperature at the start of the bed due to an overprediction of the reaction rate. If mass transfer resistances are included (MT = on) the tempature peak vanishes (see plots 2 and 4 in left column) and comparison to PRFCD results is much better.

The comparison of Fig. 7 (right) plots 1 and 2 or plots 3 and 4 suggests that the modeling of mass transfer resistance is important to predict the right species profiles. If the mass transfer resistance is included, the comparison between species profiles of 1D and 3D model is quite good. Without mass transfer resistance (Fig. 7, right, plots 2 and 4) the conversion is much too large at the beginning of the bed.

To further justify the modeling of external mass transfer resistances, the external mass-transfer Damköhler (Da) number (Eq. (60)) was evaluated for all DRM and CPOX cases (Damköhler and der Strömung, 1936). This Da number is simply the ratio of the consumption rate to maximum possible supply rate via film mass transfer.

$$\mathbf{Da} = \frac{\dot{s}_i}{C_i \bullet k_{fs,i}} \tag{60}$$

When the Da number is smaller than 1, external film resistance is directionally less important. However, when the Da number is on the order of or larger than 1, external mass transfer resistances become increasingly more important as the Da number increases.

In all DRM cases, Da numbers indicate that external mass transfer resistances are negligible (Table 11, 3rd column). For DRM the species CH_4 was selected for Da number analysis, but the same conclusions were reached if CO_2 was selected instead.

A summary of the peak Da number for O_2 in the CPOX cases is given

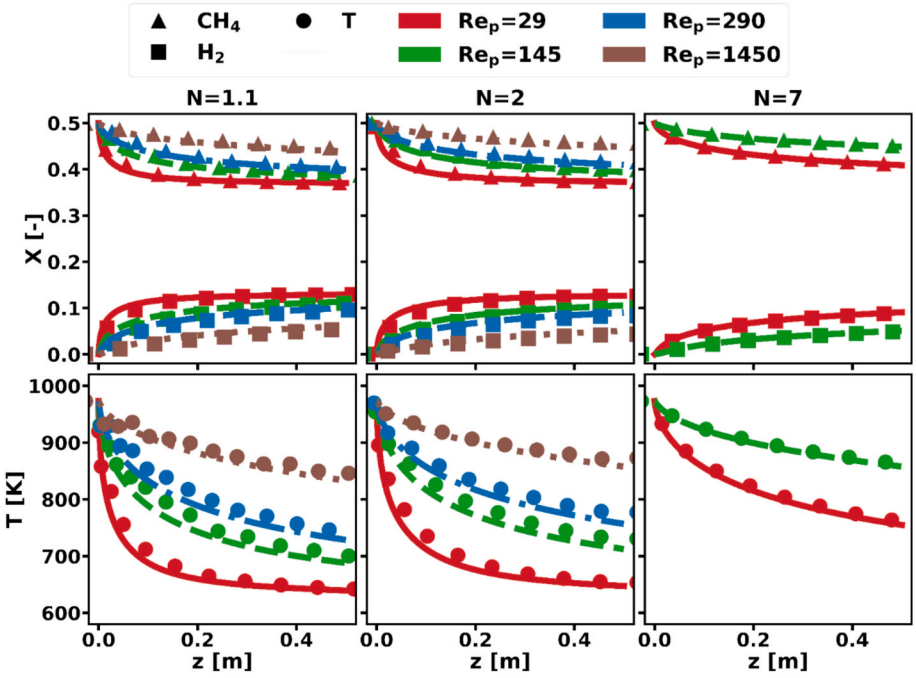

Fig. 8. Adiabatic DRM. Axial distributions of mole fractions of CH4 (▲), H2 (■), and temperature (●) profiles: 1D results (lines) vs. averaged particle-resolved 3D results (symbols) for N = 1.1, 2, 7 (columns) and$\boldsymbol{Re_p}$ = 29, 145, 290, 1450. In these plots, both the external heat transfer resistance and external mass transfer resistance models are disabled (HT = off, MT = off).

in Table 11 (4th column). O_2 is selected since the feed mixture is fuel rich and this is the most rate limiting specie. For this chemistry Da numbers were found to be generally > 1. The values of Da number decrease as N increases, due to the enhanced fluid–solid heat and mass transfer afforded by the smaller particle size as N increases (noting that the tube diameter is fixed in all cases).

As a result of these tests and the Da number analysis, all further adiabatic and non-adiabatic, non-isothermal tests with CPOX presented below included the modeling of external mass transfer resistances.

It is noted that mass transfer Sh_{fs} Methods 1 or 3 leads to a bit better agreement compared to the Method 2 for species in Fig. 9. These differences in the species plots are generally small. More importantly, the temperature profile for HT = off, MT = on (Fig. 9, left, plot 2) matches markedly better when Wakao–Kaguei Sh_{fs} Method 2 is selected. For this reason, Wakao–Kaguei Sh_{fs} Method 2 is chosen for the forthcoming non-adiabatic, non-isothermal CPOX calculations.

Meanwhile, the comparison of the temperature profiles in left column shows that the inclusion of an external heat transfer resistance model has only a small influence (compare Fig. 9, left, plots 1 and 3 or plots 2 and 4). For this reason, heat transfer resistances are disabled for the calculations with non-isothermal, non-adiabatic conditions discussed in Section 3.2.2.

Even though heat transfer resistances are not included in the non-isothermal, non-adiabatic cases that follow, it is notable that the solid temperature is higher than the fluid temperature for both PBR and PRCFD calculations. This trend is visible even though the heat of reaction is applied differently in PBR and DUO. With PBR, the heat is directly applied to the solid phase when the solid energy equation is enabled. The solid phase heats up, and then transfers heat via a resistance calculation to the fluid phase. In DUO (PRCFD), the heat of reaction is applied to the gas phase at the cell adjacent to the wall. Since the thermal conductivity of the solid is much larger than that of the gas phase, the heat is fed mainly into the solid particles.

As a result of these tests with external heat and mass transfer resistances, all further adiabatic and non-adiabatic, non-isothermal tests with CPOX presented below assume that external heat resistances can be ignored, but external mass transfer resistances are modeled using the Wakao–Kaguei Sh_{fs} Method 2 correlation.

Fig. 10 compares the results for all calculations for the conditions heat transfer off and mass transfer on (HT = off, MT = on). At N = 1.1 andRe_p = 29, rapid ignition near the inlet creates pronounced hot spots, the 3D model predicts a peak temperature close to 1150 K, about 100 K higher than the 1D result. Generally speaking, the PBR model had numerical difficulties producing stable results at N = 1.1, and the PBR result atRe_p = 29 is questionable since the equilibrium temperature is not predicted by PBR (Fig. 10, lower left plot, red line).

In all cases, more than 90% of the CH_4 converts within the first 10 cm of bed length, after which the H_2 mole fraction levels off. As Re_p rises, both CH_4 conversion and H_2 yield fall because contact time diminishes. Species predictions from the 1D and 3D models match within 5% over the full range of N and Re_p. Noticeable temperature differences arise only in low N-value beds (N ≈ 1.1–2) together with slow flow conditions ($Re_p \leq 145$). When the d_t/d_p ratio is larger (e.g., at N ≥ 7) or the flow rate is higher ($Re_p \geq 290$), the hot spot spreads axially, and the temperature profiles from the 1D and 3D models effectively overlap. It is presumed that the poorer match between 1D and 3D temperature profiles at N = 1.1 and N = 2 is due to the breakdown of the heat transfer correlations, especially at lower Re_p.

Endothermic DRM therefore demonstrates that a 1D model can reproduce temperature and species trends almost perfectly when the axial temperature gradient is gentle. Exothermic CPOX highlights the complementary limitation: The 1D model predicts global conversion for all cases accurately but under-predicts hot-spots in temperature whenever bed has a low N value and the gas moves slowly. This observation may also be due to axial conduction not being modeled by PBR, as noted in Section 2. Once N > 2 or the Re_p > 290, temperature and species discrepancies shrink below 5%, confirming that the 1D framework is fundamentally sound and needs appropriate heat- and mass-transfer correlations for full non-isothermal accuracy.

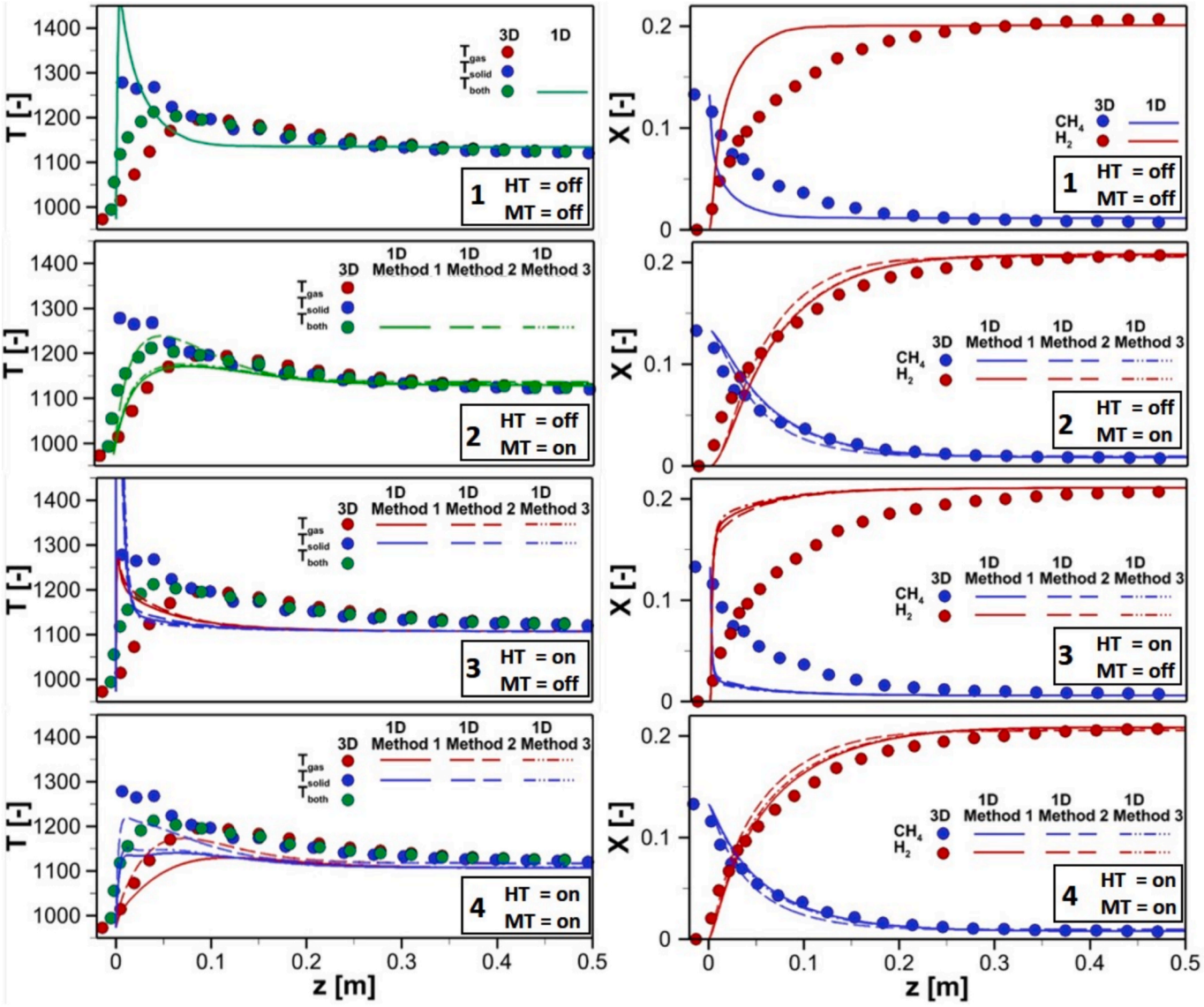

Fig. 9. Adiabatic CPOX results for N = 2, Re_p = 290 (temperature left, species right). HT = on/HT = off refers to whether external heat transfer resistance is enabled, and MT = on/MT = off denotes whether external mass transfer resistances are enabled. Method number refers to the Nu_{fs} Method (correlation) in Section 2.2.3.2.

Table 11
Peak Da values for the adiabatic DRM cases.

N	Re_p	Peak Da # for DRM	Peak Da # for CPOX
1	29	0.5	130
1	145	0.25	55
1	290	0.2	42
1	1450	0.07	17.5
2	29	0.35	65
2	145	0.2	34
2	290	0.15	24
2	1450	0.07	9
7	29	5E-3	3.7
7	145	3E-3	1.7

3.2. Non-adiabatic, non-isothermal conditions

3.2.1. Dry methane reforming (DRM)

Fig. 11 presents temperature profiles along the bed for DRM under non-isothermal conditions in three packed-bed geometries (N = 1.1, 2.0, and 7.0) and four flow regimes (Re_p = 29, 145, 290, and 1450). In each subplot, colored markers denote the 3D, particle-resolved CFD data; the thick black line is the 1D continuum prediction using the optimal heat-transfer correlations for that N–Re_p case. The faint-blue cloud shows all other 1D runs from our full sweep of correlation combinations.

Note, we also tested alternative Biot-number formulations, but found both to be essentially insensitive; accordingly, and the presented Bi formulation for all cases. Also, whenever the wall Nusselt number was calculated using Dixon-Cresswell Nu_w Method 1, Wakao–Kaguei Nu_{fs} Method 2 was selected (Dixon-Cresswell Nu_w Method 1 uses Nu_{fs} in its formulation, even though HT = off).

At the lowest flow (Re_p = 29), radial conduction dominates heat transport, producing a pronounced temperature dip just downstream of the inlet. In the lowest N-value bed (N = 1.1), the single-best combination is Dixon's blended Nu_w (Method 2), Specchia–Baldi stagnant-solid conductivity (k_{rb} Method 2), and Specchia–Baldi wall-mixing fluid conductivity (k_{rf} Method 2) (norm-RMSE = 0.088, ≈ 6 K absolute). All other correlation sets span norm-RMSEs of 0.04–0.12 (≈ 4–12 K), highlighting the sensitivity of low N-value, conduction-limited beds to small changes in both solid and fluid heat pathways.

As Re_p increases into the transitional regime (Re_p = 145–290), convective mixing mitigates conduction and the 1D cloud collapses toward the optimal curve. In the lowest N-value bed (N = 1.1), the best-fit

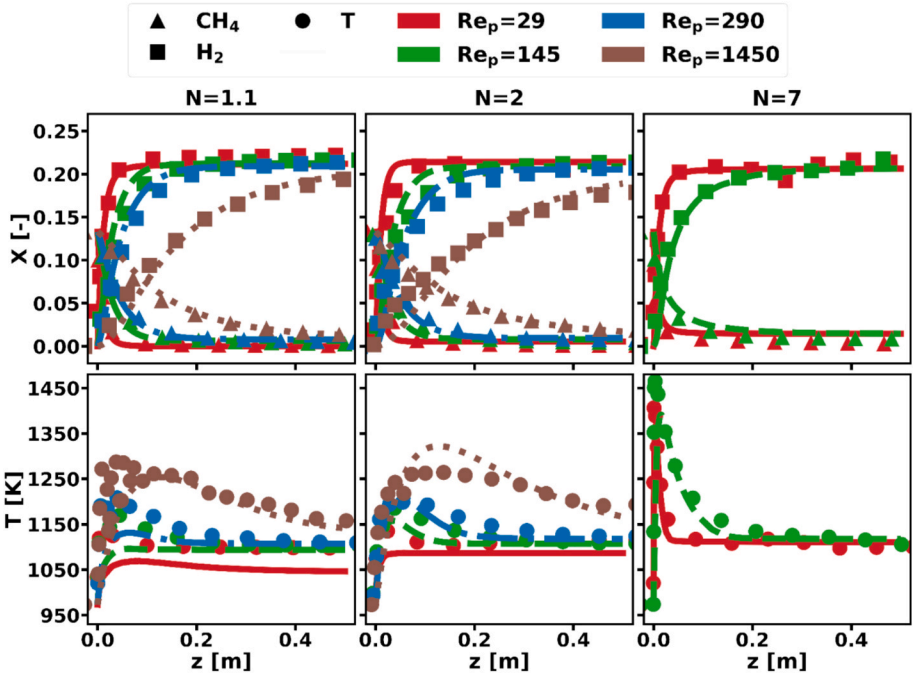

Fig. 10. Adiabatic CPOX: Axial distributions of mole fractions of CH4 (▲), H2 (■), and temperature (●) profiles: 1D results (lines) vs. averaged particle-resolved 3D results (symbols) for N = 1.1, 2, 7 (columns) and$\boldsymbol{Re_p}$ = 29, 145, 290, 1450. In these plots, external heat transfer resistance modeling is disabled, but the external mass transfer resistance model is enabled (HT = off, MT = on).

set remains Dixon's blended Nu_w (Method 2) and Specchia–Baldi solid conductivity (k_{rb} Method 2), but now uses Yagi–Wakao fluid conductivity (k_{rf} Method 1), dropping the norm-RMSE below 0.06 (≈ 4 K). In medium packings (N = 2.0), the Martin–Nilles two-term Nu_w (Method 3) becomes preferable, capturing the gentler reheating tail when using the Specchia–Baldi solid conductivity (k_{rb} Method 2) and Yagi–Wakao for k_{rf} (Method 1). In large N beds (N = 7.0 at Re_p = 145), switching to the Kunii–Smith stagnant-conduction law (k_{rb} Method 4) for k_{rs} further improves the fit and k_{rf} remains insensitive to the wall-mixing model.

In the high-Re regime (Re_p = 1450), turbulent convection overwhelms all resistances and 1D predictions tightly bracket the CFD data. In the medium-packed bed (N = 2.0), the optimal correlation set achieves a normalized RMSE of only ≈ 0.08, corresponding to an absolute RMSE of about 3–4 K, and in the lowest N-value bed (N = 1.1), a modest conduction bias persists—best-fit errors remain around 0.23 (≈ 15–20 K), and the faint-blue alternatives collapse into a very narrow band around the best-fit curve. Note, the N = 7.0 bed was simulated only up to Re_p = 145, not at Re_p = 1450. These findings confirm that for moderate-to-high flows ($Re_p \geq 290$), a single, well-validated correlation set suffices, while low Re_p still benefit from more detailed conduction-focused sub-models.

Thus, for engineering-scale 1D DRM simulations at $Re_p \geq 290$, one may adopt a single, well-validated correlation combination (blended Dixon Nu_w Method 2, with Specchia–Baldi k_{rb} Method 2, and Yagi–Wakao k_{rf} Method 1 sub-models) without significant loss of accuracy. However, in the conduction-limited regime ($Re_p \leq 50$), especially at low N values (N = 1.1 – 2.0), more detailed conduction-focused models remain necessary to keep RMSE below ≈ 6 K. The exact sub-models used for each case are listed in Table S3 of the Supplementary Information.

Fig. 12 compares the best-fit 1D simulations (lines) with 3D PRCFD results (symbols) for non-isothermal DRM across all studied conditions. The top row presents axial mole fractions of CH_4 and H_2; the bottom row shows corresponding temperature profiles. Each column corresponds to a different packing density (N = 1.1, 2.0, and 7.0), and each subplot overlays results for four particle Reynolds numbers (Re_p = 29, 145, 290, and 1450), using the optimal correlation set for each N–Re combination as determined from temperature profile matching (see Fig. 11) and detailed in Table S3-S4.

In the lowest N-value bed (N = 1.1), the 1D model accurately captures the steep thermal dip near the inlet, characteristic of conduction-limited heat transport. At Re_p = 29, the model uses Dixon's blended Nu_w (Nu_w Method 2), Specchia–Baldi for solid conductivity (k_{rb} Method 2), and Specchia–Baldi wall-mixing for fluid conductivity (k_{rf} Method 2). This reproduces the location and depth of the inlet temperature minimum with mean ΔT = 2.0 K and peak deviation under 57 K. CH_4 conversion and H_2 production profiles align within ± 5 mol %, demonstrating accurate reaction–transport coupling. As flow increases (Re_p = 145–290), switching to Yagi–Wakao (k_{rf} Method 1) for k_{rf} improves the match further, keeping mean ΔT < 2 K and species errors consistently low. At Re_p = 1450, using Bauer–Schlünder (k_{rf} Method 3) for k_{rf} improves fit under high convection, though a modest inlet bias (~23 K max) remains due to persistent conduction gradients.

In the medium-packed bed (N = 2.0), model performance improves markedly with Re_p. At Re_p = 29, using Martin–Nilles Nu_w (Method 3), Specchia–Baldi k_{rb} (Method 2), and Yagi–Wakao k_{rf} (Method 1) yields a mean ΔT = 4.0 K but a high local deviation (59 K), again caused by strong conduction bottlenecks near the inlet. At Re_p = 145 and 290, Bauer–Schlünder k_{rf}(Method 3) outperforms Yagi–Wakao (k_{rf} Method 1), reducing thermal and species RMSEs significantly—mean ΔT falls to 2.0–2.4 K, and species match remains within ± 2–3 mol %. At Re_p = 1450, using Dixon Nu_w (Method 2), Zehner–Schlünder k_{rs} (Method 1), and Winterberg–Tsotsas k_{rf} (Method 4), the 1D model nearly collapses onto the 3D reference: norm-RMSE = 0.077, mean ΔT = 1.6 K, and max deviation only 6.0 K.

In the N = 7.0 bed, evaluated at Re_p = 29 and 145, the 1D model again performs robustly. At Re_p = 29, with Dixon–Cresswell Nu_w (Method 1), Kunii–Smith k_{rb} (Method 4), and Winterberg–Tsotsas k_{rf} (Method 4), mean ΔT = 1.4 K and max deviation stays below 20 K. At Re_p = 145, the best-fit combination uses Dixon Nu_w (Method 2), Kunii–Smith k_{rb} (Method 4), and Specchia–Baldi wall-mixing k_{rf} (Method 2), yielding mean ΔT = 3.2 K and peak error = 6.1 K. CH_4 and

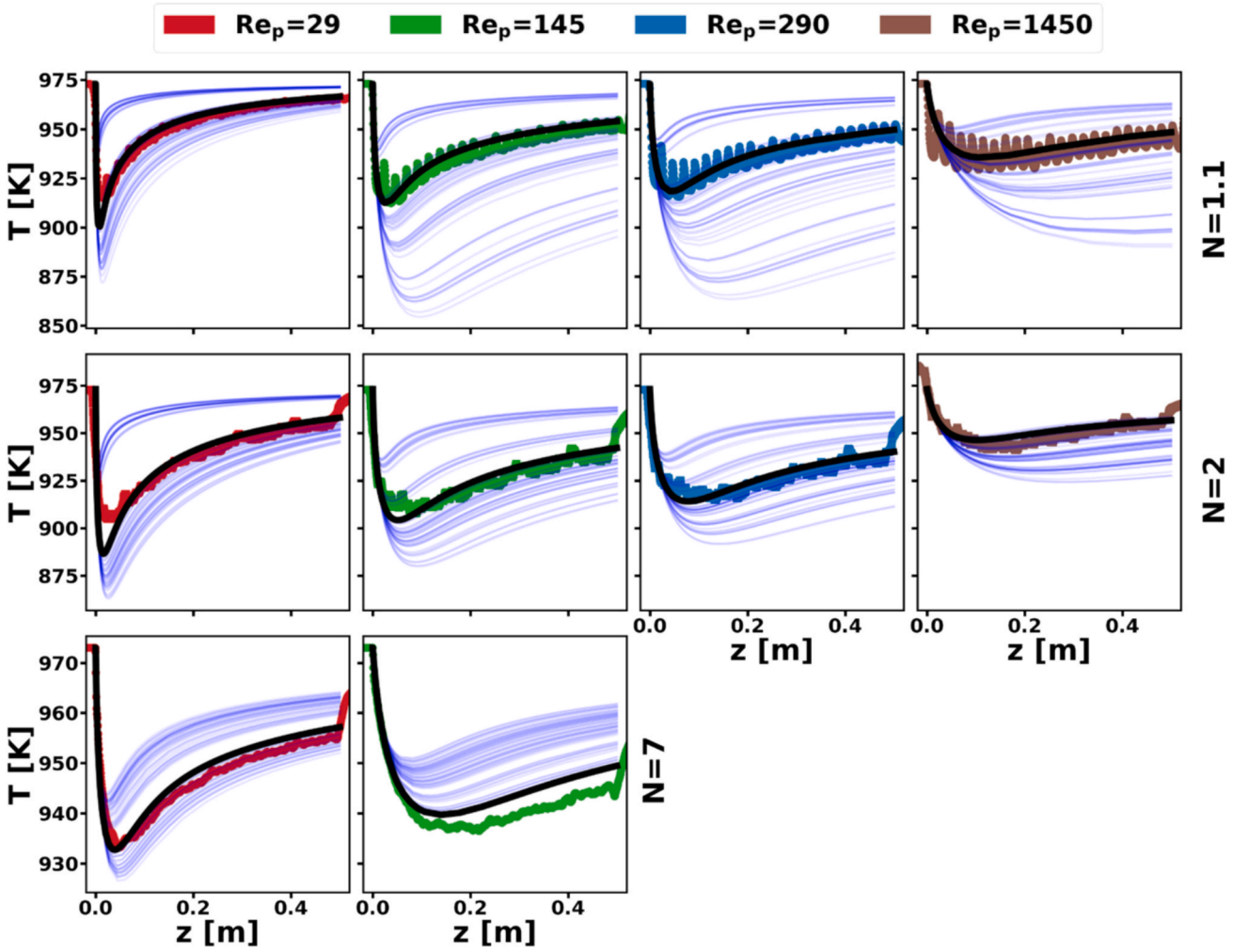

Fig. 11. Non-isothermal DRM: Axial temperature profiles, comparing 3D PRCFD (colored markers), the optimal 1D simulations (black line), and all other 1D correlation combinations (faint blue lines) for N = 1.1, 2, 7 (rows) and$\boldsymbol{Re_p}$ = 29, 145, 290, 1450 (columns). In these plots, both the external heat transfer resistance and external mass transfer resistance models are disabled (see the discussion on the selection of HT = off and MT = off in Section 3.1.1).

H_2 profiles are consistently reproduced within ± 3 mol %, confirming minimal flow-structure interaction in beds with high porosity and low conduction resistance.

Together with Fig. 11, these results validate that for each N–Re$_p$ case, a carefully selected correlation combination enables the 1D model to reproduce both reaction and heat transport trends across a wide parameter space. Even in conduction-limited regimes, the deviations remain within 2–4 K on average and rarely exceed 5 mol % for major species, affirming the robustness of the optimized submodels. However, when using a single fixed correlation set per N, as explored in Fig. S1, we observe slightly elevated discrepancies at intermediate and high Re, especially for temperature predictions in the N = 1.1 and N = 2.0 beds. These deviations arise from local mismatches in radial thermal gradients that are better captured by flow-specific correlation combinations (used in Fig. 12). Therefore, while fixed submodels per packing density (see Table S3) offer reasonable generalization across particle Reynolds numbers, flow-specific tuning remains advantageous in low N-value beds or transition-regime systems. This distinction is critical for ensuring engineering reliability in 1D simulations under varied flow conditions.

While these results validate the robustness of our correlation selection framework for the endothermic DRM case, they also highlight an important point: in DRM, the dominant heat transport challenge lies in overcoming local conduction bottlenecks, especially near the inlet, due to strong heat uptake from the highly endothermic reaction. As a result, correlations that accurately resolve solid-phase conduction (e.g., Specchia–Baldi k_{rb} Method 2, Kunii–Smith k_{rb} Method 4) and axial heat gradients become particularly crucial. However, for exothermic reactions like catalytic partial oxidation (CPOX), the local heat generation profiles shift fundamentally. Rather than cooling-induced gradients, hotspots may arise from rapid reaction zones, requiring accurate modeling of both radial heat dispersion and local convective smoothing. The following section investigates how this change in thermochemistry affects the optimal submodel combinations across Re$_p$ and packing N.

3.2.2. *Catalytic partial oxidation (CPOX)*

Fig. 13 presents axial temperature profiles for CPOX under non-isothermal conditions, comparing the best-fit 1D model predictions (black lines) with 3D, particle-resolved CFD data (colored markers) across three packing densities (N = 1.1, 2.0, 7.0) and four flow rates (Re_p = 29, 145, 290, 1450). Each subplot includes additional 1D predictions (faint blue) from alternative correlation combinations, enabling visual assessment of submodel sensitivity.

At low flow (Re_p = 29), the lowest N-value bed (N = 1.1) shows notable sensitivity to inlet hotspot representation, with the best match obtained using Dixon–Cresswell (Nu_w Method 1), Kunii-Smith (k_{rb} Method 4), and Specchia–Baldi (k_{rf}Method2; norm-RMSE ≈ 0.124). These correlations perform well in this regime due to their empirical tuning for laminar–transitional conditions and near-wall heat transport. In the medium-packed bed (N = 2.0), the same Nu_w and k_{rb} with Winterberg–Tsotsas for k_{rf} (Method 4) improves hotspot prediction,

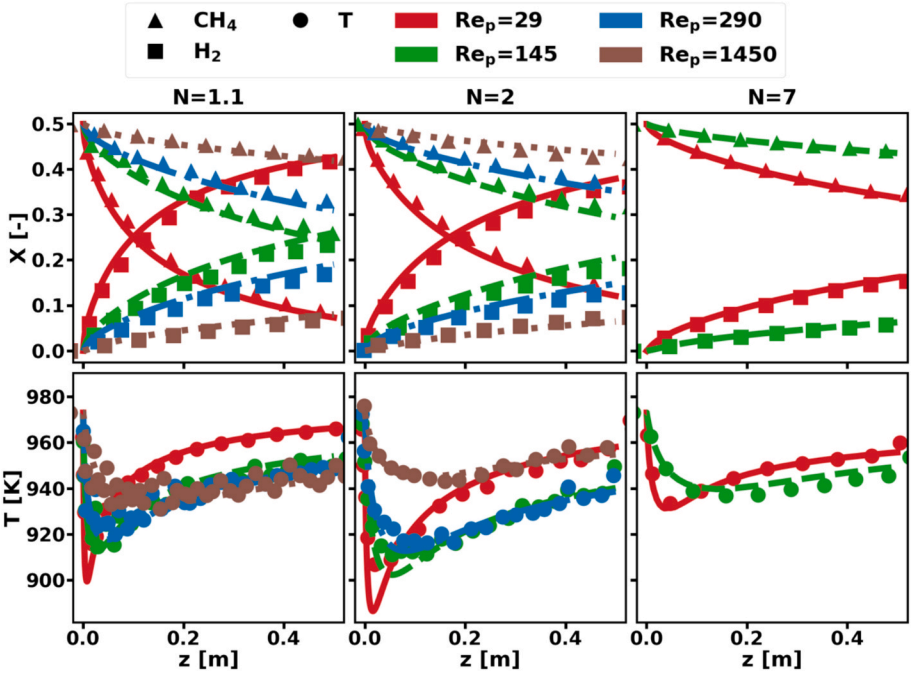

Fig. 12. Non-isothermal DRM: Axial mole fractions of CH4 (▲), H2 (■), and temperature (●) profiles: 1D lines vs. particle-resolved 3D symbols for N = 1.1, 2, 7 (columns) and$\boldsymbol{Re_p}$ = 29, 145, 290, 1450. In these plots, both the external heat transfer resistance and external mass transfer resistance models are disabled (see the discussion on the selection of HT = off and MT = off in Section 3.1.1).

lowering RMSE to ≈ 0.086. In the N = 7.0 case, the optimal combination of Martin–Nilles (Nu_w Method 3), Specchia–Baldi, and Bauer–Schlünder (k_{rf}Method 3) reproduces the narrow peak and rapid axial decay very well, yielding the lowest RMSE of ≈ 0.079.

At moderate flow (Re_p = 145), the role of radial heat transport becomes more pronounced. For N = 1.1, the best combination switches to Dixon–Cresswell (Nu_w Method 1), Specchia–Baldi (k_{rb} Method 2), and Winterberg–Tsotsas (k_{rf}Method4), effectively capturing the upstream temperature overshoot with RMSE ≈ 0.106. In the N = 2.0 bed, retaining Martin–Nilles (Nu_w Method 3) and Specchia–Baldi but switching to Winterberg–Tsotsas (k_{rf}Method4) maintains high accuracy (RMSE ≈ 0.086), reflecting the growing importance of accurate conductive scaling across solid–fluid interfaces. For N = 7.0, the best results are again delivered by blended Dixon (Nu_wMethod2), Kunii–Smith (k_{rb} Method 4), and Yagi–Wakao, demonstrating the need for stronger convective smoothing in open structures. This performance shift reflects the increased dominance of fluid-side mixing and the role of Reynolds-enhanced dispersion. At intermediate flow (Re_p = 290), the exothermic hotspot is broader and better resolved by most models. For N = 1.1, Martin–Nilles (Nu_w Method 3), Zehner–Schlünder (k_{rb} Method 1), and Specchia–Baldi (k_{rf} Method 2) yield the best fit, handling the expanded thermal zone (RMSE ≈ 0.118). For N = 2.0, the same set applies, providing good agreement with species and temperature trends (RMSE = 0.097). In N = 7.0, blended Dixon (Nu_w Method 2), Kunii–-Smith (k_{rb} Method 4), and Specchia–Baldi (k_{rf} Method 2) continue to perform well, confirming the ability of this combination to resolve radial gradients even in large N-value packed beds. The Zehner–Schlünder model (k_{rb} Method 1) in these cases benefits from its treatment of the tortuous conduction paths in dense beds and high-gradient zones.

At high flow (Re_p = 1450), turbulent convection dominates heat transfer, flattening axial gradients and spreading heat more uniformly. For N = 1.1, the best match is obtained using blended Dixon (Nu_wMethod2), Zehner–Schlünder (k_{rb}Method1), and Winterberg–Tsotsas (k_{rf}Method4). For N = 2.0, the best set is blended Dixon (Nu_wMethod2), Kunii–Smith (k_{rb} Method 4), and Bauer–Schlünder (k_{rf}Method 3), delivering norm-RMSE ≈ 0.154 and maintaining < 5 K deviation across the bed. In N = 7.0, the model with blended Dixon (Nu_wMethod2) and Kunii–Smith (k_{rb} Method 4), but switching to Yagi–Wakao for fluid-side transport (k_{rf}Method 1), delivers strong agreement with PRCFD profiles. These transitions highlight the critical role of turbulent dispersion models at high Re_p, especially Winterberg–Tsotsas (k_{rf}Method 4) and Bauer–Schlünder (k_{rf}Method 3), which are better suited to enhanced radial eddy transport. RMSEs across packings range from 0.068 to 0.173, while mean |ΔT| increases with Re, peaking around 24.5 K. Maximum local temperature deviations remain within 200–475 K, depending on flow rate and packing.

Across all packings and particle Reynolds numbers, the best-fit 1D submodel sets for CPOX simulations consistently include either Specchia–Baldi or Zehner–Schlünder for solid conductivity (k_{rb} Methods 2 and 1, respectively) and Winterberg–Tsotsas (k_{rf}Method 4) for turbulent mixing, reflecting the need for accurate modeling of localized exothermic heating zones and fast heat dissipation. Compared to the endothermic DRM case, the optimal combinations for CPOX favor stronger convective smoothing and place greater emphasis on fluid-side radial transport, in line with the thermochemical shift from heat uptake to heat release.

Fig. 14 presents axial profiles of CH_4, H_2, and temperature for the CPOX reaction under non-isothermal conditions. Each subplot compares 1D model predictions (lines) to particle-resolved 3D CFD data (symbols) for a specific packing structure (columns: N = 1.1, 2.0, 7.0) across particle Reynolds numbers Re_p = 29, 145, 290, and 1450. For each case, the 1D model uses the submodel combination identified as the most accurate based on norm-RMSE minimization (see black curve in Fig. 13 and Tables S5-S6).

For N = 1.1, the optimized correlation set evolves with increase in Re_p, Dixon–Cresswell (Nu_w Method 1), Kunii–Smith (k_{rb} Method 4), and Specchia–Baldi wall-mixing (k_{rf}Method 2) at Re_p = 29 (norm-RMSE = 0.124, mean|ΔT| ≈ 4.6 K), while higher flow rates shift the best fit toward shifting to Martin–Nilles (Nu_w Method 3) and Zehner–Schlünder solid conductivity (k_{rb}Method 1; Re_p = 290), culminating in a set of blended Dixon Nu_w (Nu_wMethod 2), Zehner–Schlünder (k_{rb} Method 1) and Winterberg–Tsotsas (k_{rf}Method 4) at Re_p = 1450. This reflects the

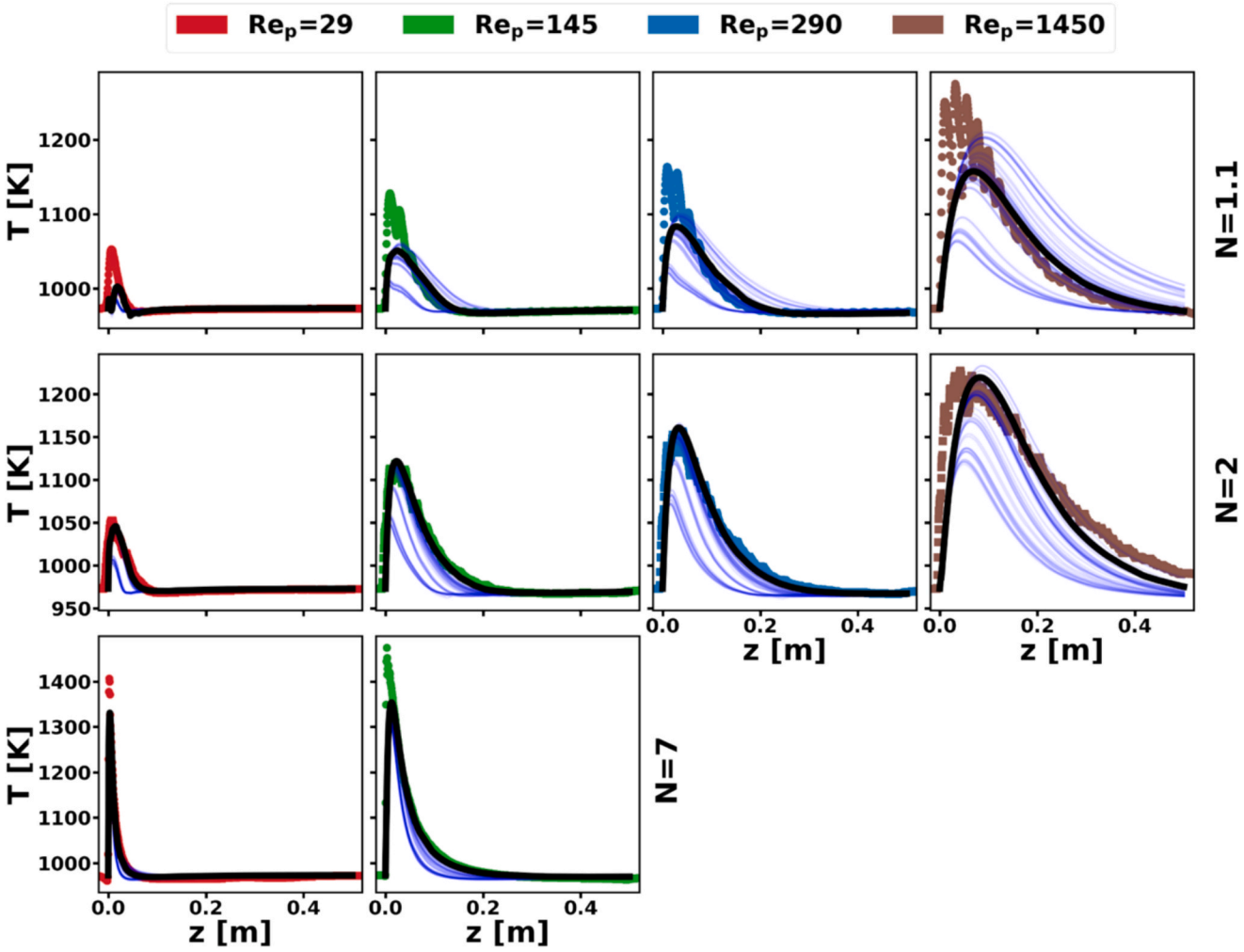

Fig. 13. Non-isothermal CPOX: Axial temperature profiles, comparing 3D PRCFD (colored markers), the optimal 1D simulations (black line), and all other 1D correlation combinations (faint blue lines) for N = 1.1, 2, 7 (rows) and $\boldsymbol{Re_p}$ = 29, 145, 290, 1450 (columns). In these plots, external heat transfer resistance modeling is disabled, but the external mass transfer resistance model is enabled (see the discussion on the selection of HT = off and MT = on in Section 3.1.2).

transition from conduction-dominated heat distribution to regimes where wall Nusselt scaling and turbulent radial mixing become critical. This adaptation effectively captures the pronounced hot spots and steep species gradients caused by exothermic heat release. The 1D model captures the CFD profiles with norm-RMSE increasing from 0.124 at Re_p = 29 to 0.173 at Re_p = 1450, while mean temperature deviations grow from 4.6 K to 24.5 K, with maximum local differences up to ~ 200 K at high flow.

For the medium-packed bed (N = 2.0), best-fit models also adapt with flow regime. At low Re_p = 29, the combination of Dixon–Cresswell (Nu_w Method 1), Kunii–Smith (k_{rb} Method 4), and Specchia–Baldi (k_{rf}Method 2) is optimal. However, at Re_p = 290, Martin–Nilles (Nu_w Method 3) and Zehner–Schlünder (k_{rb} Method 1) models yield lower RMSE. At high Re_p = 1450, the combination of blended Dixon (Nu_wMethod 2), Kunii–Smith (k_{rb} Method 4), and Bauer–Schlünder (k_{rf}Method 3) achieves the best agreement. These shifts highlight the role of both particle–wall geometry and thermochemical source terms in selecting appropriate transport correlations. RMSE values between 0.068 (Re_p = 29) and 0.154 (Re_p = 1450). Mean $|\Delta T|$ increases with Re_p from 2.7 K to 21.6 K, but peak deviations remain well below 170 K. These results demonstrate the need to tune submodels, especially at high Re where thermal gradients intensify.

In the N = 7.0 bed, the flow is distributed more uniformly, and the 1D model performs robustly across both Re_p = 29 and 1450. At Re_p = 29, blended Dixon (Nu_wMethod 2), Kunii–Smith (k_{rb} Method 4), and Specchia-Baldi wall-mixing (k_{rf}Method 2) predict the narrow thermal peak and rapid CH_4 conversion well (norm-RMSE = 0.079). At Re_p = 1450, changing k_{rf} from Specchia-Baldi (Method 2) wall-mixing to Yagi–Wakao (Method 1) method and keeping other same provides good agreement with PRCFD data. These results show that, despite intense exothermicity, high-porosity beds can be effectively modeled when turbulent mixing and conduction submodels are carefully tuned.

Across all N–Re_p combinations, 1D simulations with tailored submodel sets can reproduce both species and temperature profiles with reasonable accuracy. However, discrepancies grow with increasing Re_p, particularly in low N-value beds where steep exothermic fronts challenge classical mixing expressions. The results emphasize that CPOX modeling demands submodels capable of capturing rapid thermal evolution, strong near-wall gradients, and turbulent radial transport. Or, more pragmatically, PRCFD may remain the best solution for the analysis of low N-value beds.

With respect to heat transfer models, as compared to DRM, the CPOX system prioritizes fluid-side mixing (Winterberg–Tsotsas or Bauer–Schlünder, k_{rf}Methods 4 and 3 respectively) and near-wall conductivity (Specchia–Baldi, k_{rf}Method 2), highlighting the importance of thermochemistry-driven model selection for accurate reactor-scale predictions.

These trends also reflect the underlying physics embedded in each

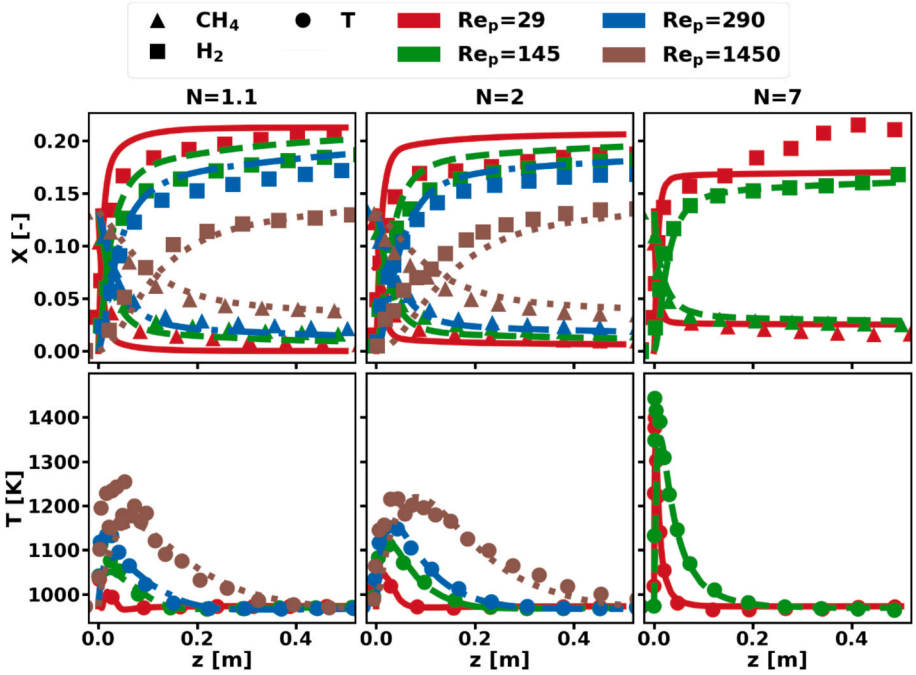

Fig. 14. Non-isothermal CPOX: Axial mole fractions of CH4 (▲), H2 (■), and temperature (●) profiles: 1D lines vs. particle-resolved 3D symbols for N = 1.1, 2, 7 (columns) and$\boldsymbol{Re_p}$ = 29, 145, 290, 1450. In these plots, external heat transfer resistance modeling is disabled, but the external mass transfer resistance model is enabled (see the discussion on the selection of HT = off and MT = on in Section 3.1.2).

correlation. For example, the Specchia–Baldi wall-mixing model (k_{rf}Method 2) explicitly accounts for near-wall turbulence damping, which becomes critical under high exothermicity. Similarly, the Winterberg–Tsotsas model (k_{rf}Method 4), derived from superposition of axial and radial eddies, provides stronger radial mixing than classical Yagi–Wakao (k_{rf}Method1) or Specchia-type (k_{rf}Method 2) expressions, making it ideal for capturing CPOX-induced hot spots. In contrast, Zehner–Schlünder's (k_{rb} Method 1) conduction model, which includes tortuosity and contact resistance, performs better at high particle Reynolds numbers and high N-value packings due to its effective smoothing of sharp thermal spikes. These mechanistic differences help explain the distinct optimal model choices across flow regimes and reaction systems.

Comparing Fig. 12 and Fig. 14 shows a fundamental contrast in the thermal modeling demands posed by the endothermic DRM and exothermic CPOX systems. In DRM, heat is continuously consumed by the strongly endothermic reactions, producing relatively smooth and predictable thermal gradients. As a result, accurate temperature prediction can be achieved with moderate correlation tuning, as reflected in the low mean $|\Delta T|$ values (typically < 5 K) and normalized RMSEs generally below 0.15 across all N–Re cases.

In contrast, CPOX introduces intense and localized heat release near the inlet, leading to sharp thermal gradients and strong radial non-uniformities that challenge classical heat transfer models. This is evident from significantly higher discrepancies: mean $|\Delta T|$ exceeds 20 K in low N-value beds (N = 1.1) at $Re_p = 1450$, and local temperature deviations surpass 400 K in high N-value configurations (e.g., N = 7.0, $Re_p = 145$). These observations highlight the greater complexity of resolving exothermic heat transport, where convective dispersion, local reaction rates, and turbulence interact more dynamically.

CPOX simulations are therefore more sensitive to submodel selection, particularly for fluid-phase radial conductivity and wall heat transfer. Whereas DRM simulations primarily depend on solid-phase conduction and moderate axial smoothing, CPOX demands robust treatment of turbulent mixing, near-wall eddy transport, and thermal feedback mechanisms. This contrast highlights the important role of reaction thermochemistry in guiding submodel choices and strengthens the case for reaction-specific correlation optimization in reactor-scale simulations.

4. Discussion

For new 1D reactor simulations where no experimental data or PRCFD reference is available, the present results provide some insight into which heat transfer models should be selected based on simple geometric and operating indicators (N, Re, and reaction thermochemistry). For high N-value beds (where most packed bed reactors operate), general guidance based on the present results is provided in Table S7 for 1D heat transfer modeling when validation data do not exist. Similar guidance is given for modeling of low N-value beds in Table S8.

Some trends in Tables S7 and S8 are somewhat counterintuitive, especially when viewed through the narrow validity ranges originally reported for several correlations. For example, correlations such as Dixon-Cresswell for the wall Nusselt number (Nu_w Method 1) and Zehner-Schlünder for the solid-phase conductivity (k_{rb} Method 1) were derived for more conventional beds and parameter windows, yet in this study they often remained competitive even in slender, strongly inhomogeneous packings where one might expect them to fail more severely. Conversely, correlations like the Martin-Nilles wall model (Nu_w Method 3), which are widely used for design calculations, did not always provide the most robust choice once strong reaction-driven temperature gradients and low N or low Re conditions were considered, despite their good performance in the original, higher-N datasets. These outcomes emphasize that correlation performance outside its nominal database cannot be inferred solely from the original fit range, and that interaction with reaction thermochemistry and bed characteristics can be as important as matching Re_p and N. This implies that when developing new heat transfer correlations for packed bed reactors, it may be beneficial to develop such correlations with data from reactive, rather than non-reactive systems. The present work suggests that correlations developed from reactive PRCFD would further depend on the exo/endothermicity of the reaction, and the presence of strong temperature gradients.

Because the PRCFD particles are geometrically shrunk, there is no

solid–solid contact conduction in the reference 3D PRCFD simulations. As a result, all interparticle heat exchange proceeds through the fluid in these cases. This has two main implications for 1D model selection and validation. First, any k_{rb} correlation that relies strongly on solid contact networks (e.g., high-conductivity, tightly packed beds) will overpredict radial conduction relative to the PRCFD baseline. Second, wall–bed heat transfer in the PRCFD case is likewise biased toward fluid-mediated mechanisms, so 1D combinations that emphasize fluid-side dispersion and wall Nusselt numbers consistent with purely convective contact are more directly comparable. Overall, 1D-3D PRCFD agreement under these conditions validates the effective "no-contact" parameter set for similar slender beds, but does not guarantee accuracy for real reactors where particle bridges and wall contacts contribute significantly to heat conduction. Another meshing strategy is to apply bridges, so long as the thermal conductivity of the bridges are managed (Dixon et al., 2013).

With respect to external heat and mass transfer resistances, CPOX was particularly susceptible to O_2 external mass transfer resistance, especially near the start of the bed where this species is rapidly consumed. The inclusion of external mass transfer resistance in the PBR models was further justified by a Damköhler Number analysis at N = 1 and N = 2 (the N = 7 results were generally the same no matter whether external mass transfer resistances were modeled, or not). However, a series of adiabatic cases run with external heat transfer resistances showed that the inclusion of this effect had only a small impact on DRM and CPOX results at N = 1 and N = 2, and effectively no impact at N = 7 for both chemistries. All tested Nu_{fs} (or Sh_{fs}) correlations produced similar results, and so whenever a Nu_{fs} (or Sh_{fs}) correlation was required, the correlation of Wakao–Kaguei (Nu_{fs} Method 2) was selected.

5. Conclusions

This study presents a detailed comparison of 1D continuum and 3D particle-resolved simulations for catalytic fixed-bed reactors under non-isothermal conditions. By systematically screening submodels for wall heat transfer (Nu_w), bed (solid) conductivity (k_{rb}), and radial fluid conductivity (k_{rf}), we identify optimal combinations for both endothermic DRM and exothermic CPOX reactions across a wide range of particle Reynolds numbers and packing densities.

For DRM, submodels prioritizing solid-phase conduction and moderate radial mixing (e.g., Specchia–Baldi, Yagi–Wakao) capture the smooth thermal gradients with mean temperature errors below 5 K. In contrast, CPOX simulations require submodels that resolve sharp thermal fronts and turbulent dispersion—particularly near the inlet—where models such as Winterberg–Tsotsas and Bauer–Schlünder (k_{rf} Methods 4 and 3, respectively) demonstrate superior performance.

We find that no single correlation set performs best across all conditions for the DRM and CPOX cases studied. However, for a given packing density, a fixed set can offer robust performance across Re, with minimal error growth. These findings highlight the importance of thermochemistry-specific submodel tuning and provide practical guidance for selecting transport correlations in reactor-scale 1D simulations. Our results underscore the need to account for local heat generation, turbulence, and packing geometry to achieve predictive accuracy without resorting to overparameterization.

CRediT authorship contribution statement

Akash Shirsath: Writing – original draft, Visualization, Validation, Methodology, Investigation, Data curation, Conceptualization. **Matthias Hettel:** Writing – original draft, Visualization, Validation, Methodology, Investigation, Data curation, Conceptualization. **Eric A. Daymo:** Conceptualization, Formal analysis, Investigation, Methodology, Software, Validation, Writing – original draft. **Martin Kutscherauer:** Writing – original draft, Methodology, Formal analysis. **Olaf Deutschmann:** Resources.

Declaration of competing interest

The authors declare that they have no known competing financial interests or personal relationships that could have appeared to influence the work reported in this paper.

Acknowledgements

A cost-free academic license of DETCHEM^{TM} by the Omegadot Software & Consulting GmbH (www.omegadot.software) is gratefully acknowledged. The calculations were performed on the HPC resource bwUniCluster (2.0), funded by the Ministry of Science, Research and the Arts Baden-Württemberg and the Universities of the State of Baden-Württemberg. The authors acknowledge support by the state of Baden-Württemberg through bwHPC.

Appendix A. Supplementary data

Supplementary data to this article can be found online at https://doi.org/10.1016/j.ces.2026.124172.

Data availability

Data will be made available on request.

References

Eigenberger, G., Werther, J., Schoenfelder, H., Beenackers, A.A.C.M., St, Y., Matros, G.A., Bunimovich, G., Donati, N., Habashi, I., Miracca, D.S., 1997. Reaction engineering. In: Ertl, G., Knözinger, H., Weitkamp, J. (Eds.), Handbook of Heterogeneous Catalysis. Wiley-VCH Verlag GmbH, Weinheim, Germany.

Deutschmann, O., Schmidt, L.D., 1998. Modeling the partial oxidation of methane in a short-contact-time reactor. AIChE J. 44, 2465–2477. https://doi.org/10.1002/aic.690441114.

Schwiedernoch, R., Tischer, S., Correa, C., Deutschmann, O., 2003. Experimental and numerical study on the transient behavior of partial oxidation of methane in a catalytic monolith. Chem. Eng. Sci. 58, 633–642. https://doi.org/10.1016/S0009-2509(02)00589-4.

Giehr, A., Maier, L., Angeli, S., Schunk, S.A., Deutschmann, O., 2020. Dry and steam reforming of CH4 on co-hexaaluminate: on the formation of metallic co and its influence on catalyst activity. Ind. Eng. Chem. Res. 59, 18790–18797. https://doi.org/10.1021/acs.iecr.0c03522.

Dixon, A.G., Wu, Y., 2020. Partial oxidation of o-xylene to phthalic anhydride in a fixed bed reactor with axial thermowells. Chem. Eng. Res. Des. 159, 125–137. https://doi.org/10.1016/j.cherd.2020.03.027.

Ziółkowska, I., Ziółkowski, D., 1988. Fluid flow inside packed beds. Chem. Eng. Process. 23, 137–164. https://doi.org/10.1016/0255-2701(88)80012-6.

Giese, M., Rottschäfer, K., Vortmeyer, D., 1998. Measured and modeled superficial flow profiles in packed beds with liquid flow. AIChE J. 44, 484–490. https://doi.org/10.1002/aic.690440225.

Dixon, A.G., 2021a. Local transport and reaction rates in a fixed bed reactor tube: exothermic partial oxidation of ethylene. Chem. Eng. Sci. 231, 116305. https://doi.org/10.1016/j.ces.2020.116305.

Dixon, A.G., 2021b. Local structure effects on heat transfer in very low tube-to-particle diameter ratio fixed beds of spheres. Ind. Eng. Chem. Res. 60, 9777–9786. https://doi.org/10.1021/acs.iecr.1c01660.

Kutscherauer, M., Anderson, S.D., Böcklein, S., Mestl, G., Turek, T., Wehinger, G.D., 2024. A conjugated heat and mass transfer model to implement reaction in particle-resolved CFD simulations of catalytic fixed bed reactors. Eng. Appl. Comput. Fluid Mech. 18, 2292100. https://doi.org/10.1080/19942060.2023.2292100.

Freund, H., Bauer, J., Zeiser, T., Emig, G., 2005. Detailed simulation of transport processes in fixed-beds. Ind. Eng. Chem. Res. 44, 6423–6434. https://doi.org/10.1021/ie0489453.

Froment, G.F., De Wilde, J., Bischoff, K.B., 2011. Chemical reactor analysis and design, 3rd ed. Wiley, Hoboken, N.J.

Stegehake, C., Riese, J., Grünewald, M., 2019. Modeling and validating fixed-bed reactors: a state-of-the-art review. ChemBioEng. Rev. 6, 28–44. https://doi.org/10.1002/cben.201900002.

Flaischlen, S., Wehinger, G.D., 2019. Synthetic packed-bed generation for CFD simulations: blender vs STAR-CCM+. Chem. Eng. 3, 52. https://doi.org/10.3390/chemengineering3020052.

Jurtz, N., Kraume, M., Wehinger, G.D., 2019. Advances in fixed-bed reactor modeling using particle-resolved computational fluid dynamics (CFD). Rev. Chem. Eng. 35, 139–190. https://doi.org/10.1515/revce-2017-0059.

Dixon, A.G., Partopour, B., 2020. Computational fluid dynamics for fixed bed reactor design. Annu. Rev. Chem. Biomol. Eng. 11, 109–130. https://doi.org/10.1146/annurev-chembioeng-092319-075328.
Jurtz, N., Waldherr, P., Kraume, M., 2019. Numerical analysis of the impact of particle friction on bed voidage in fixed-beds. Chem. Ing. Tech. 91, 1260–1266. https://doi.org/10.1002/cite.201800190.
Partopour, B., Dixon, A.G., 2017. An integrated workflow for resolved-particle packed bed models with complex particle shapes. Powder Technol. 322, 258–272. https://doi.org/10.1016/j.powtec.2017.09.009.
Wehinger, G.D., Klippel, F., Kraume, M., 2017. Modeling pore processes for particle-resolved CFD simulations of catalytic fixed-bed reactors. Comput. Chem. Eng. 101, 11–22. https://doi.org/10.1016/j.compchemeng.2017.02.029.
Dixon, A.G., Taskin, M.E., Nijemeisland, M., Stitt, E.H., 2010. CFD method to couple three-dimensional transport and reaction inside catalyst particles to the fixed bed flow field. Ind. Eng. Chem. Res. 49, 9012–9025. https://doi.org/10.1021/ie100298q.
Maffei, T., Gentile, G., Rebughini, S., Bracconi, M., Manelli, F., Lipp, S., Cuoci, A., Maestri, M., 2016. A multiregion operator-splitting CFD approach for coupling microkinetic modeling with internal porous transport in heterogeneous catalytic reactors. Chem. Eng. J. 283, 1392–1404. https://doi.org/10.1016/j.cej.2015.08.080.
Wehinger, G.D., Ambrosetti, M., Cheula, R., Ding, Z.-B., Isoz, M., Kreitz, B., Kuhlmann, K., Kutscherauer, M., Niyogi, K., Poissonnier, J., Réocreux, R., Rudolf, D., Wagner, J., Zimmermann, R., Bracconi, M., Freund, H., Krewer, U., Maestri, M., 2022. Quo vadis multiscale modeling in reaction engineering? - A perspective. Chem. Eng. Res. Des. 184, 3958. https://doi.org/10.1016/j.
Bukowski, B.C., Keil, F.J., Ravikovitch, P.I., Sastre, G., Snurr, R.Q., Coppens, M.-O., 2021. Connecting theory and simulation with experiment for the study of diffusion in nanoporous solids. Adsorption 27, 683–760. https://doi.org/10.1007/s10450-021-00314-y.
Pope, S.B., 1997. Computationally efficient implementation of combustion chemistry using in situ adaptive tabulation. Combust. Theor. Model. 1, 41–63. https://doi.org/10.1080/713665229.
Babajimopoulos, A., Assanis, D.N., Flowers, D.L., Aceves, S.M., Hessel, R.P., 2005. A fully coupled computational fluid dynamics and multi-zone model with detailed chemical kinetics for the simulation of premixed charge compression ignition engines. Int. J. Engine Res. 6, 497–512. https://doi.org/10.1243/146808705X30503.
Döppel, F.A., Votsmeier, M., 2022. Efficient machine learning based surrogate models for surface kinetics by approximating the rates of the rate-determining steps. Chem. Eng. Sci. 262, 117964. https://doi.org/10.1016/j.ces.2022.117964.
Bracconi, M., Maestri, M., 2020. Training set design for machine learning techniques applied to the approximation of computationally intensive first-principles kinetic models. Chem. Eng. J. 400, 125469. https://doi.org/10.1016/j.cej.2020.125469.
Biermann, F., Uglietti, R., Döppel, F.A., Kircher, T., Bracconi, M., Maestri, M., Votsmeier, M., 2025. Enabling micro-kinetics based simulation of industrial packed-bed reactors by physics-enhanced neural networks. Chem. Eng. J. 519, 163598. https://doi.org/10.1016/j.cej.2025.163598.
Dixon, A.G., 2026. Recent developments in the application of particle-resolved CFD to fixed-bed reactors. Curr. Opin. Chem. Eng. 51, 101225. https://doi.org/10.1016/j.coche.2025.101225.
Anderson, S.D., Kutscherauer, M., Böcklein, S., Mestl, G., Turek, T., Wehinger, G.D., 2023. Investigating the accuracy of continuum models for the simulation of industrial maleic anhydride reactors: a comparative single particle CFD study. Chem. Eng. Res. Des. 200, 655–669. https://doi.org/10.1016/j.cherd.2023.11.018.
Hernandez-Aguirre, A., Hernandez-Rodriguez, R., Ochoa-Tapia, J.A., Castillo-Araiza, C. O., 2025. Development of a generalized pseudo-continuous model for fluid dynamics in packed bed reactors with a low Dt/Dp. Chem. Eng. J. 510, 161298. https://doi.org/10.1016/j.cej.2025.161298.
Liu, W., Chen, G., Zheng, D., Ge, M., Liu, C., 2023. An improved anisotropic continuum model for the flow and heat transfer in grain aeration system. J. Food Process Eng 46, e14421. https://doi.org/10.1111/jfpe.14421.
Weng, J., Wen, S., Shu, Z., Jiang, J., Ye, G., Zhou, X., 2025. A 2D continuum model based on particle-resolved CFD for packed-bed reactors. Ind. Eng. Chem. Res. 64, 8516–8530. https://doi.org/10.1021/acs.iecr.5c00351.
Xavier, K., Kusum Kumar, B., Khan, M.S., Tiwari, S.S., Goyal, H., 2026. Modeling fixed bed reactors as porous media using unit cell simulations. Chem. Eng. Sci. 320, 122592. https://doi.org/10.1016/j.ces.2025.122592.
Benzinger, W., Daymo, E., Hettel, M., Maier, L., Antinori, C., Pfeifer, P., Deutschmann, O., 2019. Reverse water gas shift (RWGS) over Ni – spatially-resolved measurements and simulations. Chem. Eng. J. 362, 430–441. https://doi.org/10.1016/j.cej.2019.01.038.
Deutschmann, O., Tischer, S., Correa, C., Chatterjee, D., Kleditzsch, S., Janardhanan, V. M., Mladenov, N., Minh, H.D., Karadeniz, H., Hettel, M., 2014. DETCHEM Software package, www.detchem.com, Karlsruhe, Germany.
Hettel, M., Wörner, M., Deutschmann, O., 2018. Computational fluid dynamics of catalytic reactors. In: Andreoni, W., Yip, S. (Eds.), Handbook of Materials Modeling: Applications: Current and Emerging Materials. Springer International Publishing, Cham, pp. 1–34. https://doi.org/10.1007/978-3-319-50257-1_6-1.
Kee, R.J., Coltrin, M.E., Glarborg, P., 2003. Chemically reacting flow, theory and practice. A John Wiley & Sons Publication, Wiley.
Daymo, E.A., Hettel, M., Deutschmann, O., Wehinger, G.D., 2022. Accelerating particle-resolved CFD simulations of catalytic fixed-bed reactors with DUO. Chem. Eng. Sci. 250, 117408. https://doi.org/10.1016/j.ces.2021.117408.
Hettel, M., Daymo, E., Deutschmann, O., 2018. 3D modeling of a CPOX-reformer including detailed chemistry and radiation effects with DUO. Comput. Chem. Eng. 109, 166–178. https://doi.org/10.1016/j.compchemeng.2017.11.005.
Hettel, M., Diehm, C., Bonart, H., Deutschmann, O., 2015. Numerical simulation of a structured catalytic methane reformer by DUO: the new computational interface for OpenFOAM® and DETCHEM™. Catal. Today 258, 230–240. https://doi.org/10.1016/j.cattod.2015.02.011.
Deutschmann, O., 2011. Modeling and simulation of heterogeneous catalytic reactions: from the molecular process to the technical system. Wiley-VCH Weinheim.
Deutschmann, O., Schwiedemoch, R., Maier, L.I., Chatterjee, D., 2001. Natural gas conversion in monolithic ceeatalysts: interaction of chemical reactions and transport phenomena. In: Iglesia, E., Spivey, J.J., Fleisch, T.H. (Eds.), Studies in Surface Science and Catalysis. Elsevier, pp. 251–258. https://doi.org/10.1016/S0167-2991(01)80312-8.
Delgado, K.H., Maier, L., Tischer, S., Zellner, A., Stotz, H., Deutschmann, O., 2015. Surface reaction kinetics of steam- and CO2-reforming as well as oxidation of methane over nickel-based catalysts. Catalysts 871–904. https://doi.org/10.3390/catal5020871.
Wehinger, G.D., Kraume, M., Berg, V., Korup, O., 2016. Investigating dry reforming of methane with spatial reactor profiles and particle-resolved CFD simulations. AIChE J. 62, 4436–4452. https://doi.org/10.1002/aic.15520.
Ergun, S., 1952. Fluid flow through packed columns. Chem. Eng. Prog. 48, 89–94.
Zehner, P., Schlünder, E.U., 1970. Wärmeleitfähigkeit von Schüttungen bei mäßigen Temperaturen. Chem. Ing. Tech. 42, 933–941. https://doi.org/10.1002/cite.330421408.
Specchia, V., Baldi, G., Sicardi, S., 1980. Heat transfer in packed bed reactors with one phase flow. Chem. Eng. Commun. 4, 361–380. https://doi.org/10.1080/00986448008935916.
Bauer, R., Schlunder, E.U., 1978. Effective radial thermal conductivity of packings in gas flow. Part I. Convective transport coefficient. Int. Chem. Eng. 18, 189–204.
Kunii, D., Smith, J.M., 1960. Heat transfer characteristics of porous rocks. AIChE J. 6, 71–78. https://doi.org/10.1002/aic.690060115.
Yagi, S., Wakao, N., 1959. Heat and mass transfer from wall to fluid in packed beds. AIChE J. 5, 79–85. https://doi.org/10.1002/aic.690050118.
Winterberg, M., Tsotsas, E., Krischke, A., Vortmeyer, D., 2000. A simple and coherent set of coefficients for modelling of heat and mass transport with and without chemical reaction in tubes filled with spheres. Chem. Eng. Sci. 55, 967–979. https://doi.org/10.1016/S0009-2509(99)00379-6.
Melanson, M.M., Dixon, A.G., 1985. Solid conduction in low dt/dp beds of spheres, pellets and rings. Int. J. Heat Mass Transf. 28, 383–394. https://doi.org/10.1016/0017-9310(85)90071-7.
Dixon, A.G., 1988. Wall and particle-shape effects on heat transfer in packed beds. Chem. Eng. Commun. 71, 217–237. https://doi.org/10.1080/00986448808940426.
Maxwell, J.C., 1873. A treatise on electricity and magnetism, Clarendon press.
Dixon, A.G., Cresswell, D.L., 1979. Theoretical prediction of effective heat transfer parameters in packed beds. AIChE J. 25, 663–676. https://doi.org/10.1002/aic.690250413.
Wakao, N., Kagei, S., 1982. Heat and mass transfer in packed beds. Taylor & Francis.
Dixon, A.G., 2012. Fixed bed catalytic reactor modelling-the radial heat transfer problem. Can. J. Chem. Eng. 90, 507527. https://doi.org/10.1002/cjce.21630.
Martin, H., Nilles, M., 1993. Radiale Wärmeleitung in durchströmten Schüttungsrohren. Chemie Ingenieur Technik - CIT 65, 1468–1477. https://doi.org/10.1002/cite.330651206.
Gnielinski, V., 2010. VDI heat atlas. VDI Heat Atlas 9–10. https://doi.org/10.1007/978-3-540-77877-6.
Nuclear Safety Standards, C., 1983. Reactor core design of high-temperature gas-cooled reactors part 2: heat transfer in spherical fuel elements, Safety Standards of the Nuclear Safety Standards Comission (KTA), 3102.2, 1-5.
Dixon, A.G., 1996. An improved equation for the overall heat transfer coefficient in packed beds. Chem. Eng. Process. 35, 323–331. https://doi.org/10.1016/0255-2701(96)80012-2.
Incropera, F.P.D., David, P., 1996. Fundamentals of heat and mass transfer, 4th Edition ed.,. John Wiley & Sons, Inc.
Mokashi, M., Shirsath, A.B., Çelik, A., Lott, P., Müller, H., Tischer, S., Maier, L., Bode, J., Schlereth, D., Scheiff, F., Flick, D., Bender, M., Ehrhardt, K., Deutschmann, O., 2024. Methane pyrolysis in packed bed reactors: kinetic modeling, numerical simulations, and experimental insights. Chem. Eng. J. 485, 149684. https://doi.org/10.1016/j.cej.2024.149684.
Shirsath, A.B., Schulte, M.L., Kreitz, B., Tischer, S., Grunwaldt, J.-D., Deutschmann, O., 2023. Spatially-resolved investigation of CO2 methanation over Ni/γ-Al2O3 and Ni3.2Fe/γ-Al2O3 catalysts in a packed-bed reactor. Chem. Eng. J. 469, 143847. https://doi.org/10.1016/j.cej.2023.143847.
Deuflhard, P., Hairer, E., Zugck, J., 1987. One-step and extrapolation methods for differential-algebraic systems. Numer. Math. 51, 501–516. https://doi.org/10.1007/BF01400352.
OpenFOAM, 2017. The Open Source CFD Toolbox.
Dixon, A.G., 2017. Local transport and reaction rates in a fixed bed reactor tube: endothermic steam methane reforming. Chem. Eng. Sci. 168, 156–177. https://doi.org/10.1016/j.ces.2017.04.039.

Daymo, E.A., Hettel, M., 2026. Fixed bed reactor modeling with internal and external transport resistances: comparing 3D PRCFD and 2D porous media simulations. Chem. Eng. Sci. 321, 122779. https://doi.org/10.1016/j.ces.2025.122779.

Damköhler, G., der Strömung, E., 1936. Diffusion und des Wärmeüberganges auf die Leistung von Reaktionsöfen.: I. Allgemeine Gesichtspunkte für die übertragung eines chemischen Prozesses aus dem Kleinen ins Große. Zeitschrift Für Elektrochemie Und Angewandte Physikalische Chemie 42, 846–862. https://doi.org/10.1002/bbpc.19360421203.

Dixon, A.G., Nijemeisland, M., Stitt, E.H., 2013. Systematic mesh development for 3D CFD simulation of fixed beds: contact points study. Comput. Chem. Eng. 48, 135–153. https://doi.org/10.1016/j.compchemeng.2012.08.011.